

# Eurasian fundamental mode surface wave phase velocities and their relationship with tectonic structures

Andrew Curtis,<sup>1</sup> Jeannot Trampert, Roel Snieder

Department of Theoretical Geophysics, Utrecht University, Utrecht, Netherlands

Bernard Dost

Observatories and Research Facilities for European Seismology (ORFEUS Data Center), De Bilt, Netherlands

**Abstract.** We automatically analyzed 32,000 fundamental mode Love and Rayleigh wave signals with earthquake–station paths traversing Eurasia and Indonesia and obtained robust average phase velocity measurements between 20 s and 170 s periods along 4389 Love and 4020 Rayleigh paths. These were inverted to give phase velocity maps at 14 fixed periods. Resolution tests suggest that features with diameter >750 km and >500 km are resolved over most of Eurasia and central/SE Asia respectively. Low-period Love waves image areas with thick sedimentary cover as low-velocity zones, and almost all periods image mountainous regions since these have thick crust and hence low average lithospheric shear velocity. At long periods, both Love and Rayleigh waves define high phase velocity zones across shield and cratonic areas reflecting their deep lithospheric roots. We observe significant along-strike heterogeneity in the Zagros fold belt and Tien Shan–Altai system. Taking sections across Eurasian phase velocity space allows us to make approximate interpretations in terms of shear velocity structure directly. For example, the Red River and East Vietnam Boundary faults are traced on their eastern side by low velocities which extend at depth into Indonesia. We relate this to mantle upwelling associated with early Eocene rotation of Indochina and reversal of the sense of shear across the Red River fault post-20 Ma. We observe dipping subduction of the Mediterranean beneath the Aegean, of the Philippine Sea beneath Indonesia, and of the Indian shield beneath Tibet. We also image a fossil subducted plate beneath NE Borneo which we associate with subduction of the proto-South China Sea between 50 Ma and 15 Ma.

## 1. Introduction

For more than 10 years, normal mode and surface wave seismologists have used automated data processing techniques to construct global velocity models from huge volumes of digital data accumulated across the Global Digital Seismographic Network (GDSN) [e.g., Woodhouse and Dziewonski, 1984; Zang and Tanimoto, 1993; Trampert and Woodhouse, 1995, 1996; Ekström *et al.*, 1997]. Global studies suffer, however, from diminished lateral resolution caused by the unsuitable geometry of paths along which reliable surface wave dispersion measurements can be obtained. This is especially lim-

iting in the oceans, which generally support relatively small earthquakes confined to narrow ridges or subduction zones with very few recording stations; as a consequence, two thirds of the Earth's surface is traversed almost exclusively by long event–station paths. When dispersion data along all paths are inverted into global models of phase or shear velocity, the reduced resolution in oceanic areas also effects the continental areas of global models in two ways: (1) continental structure may be mapped erroneously into the relatively unconstrained oceans due to the global least squares procedure usually employed in the inversion scheme, and (2) global spherical harmonic basis functions are usually used to represent the structure, introducing a direct correlation between oceanic and continental structure which might have a significant effect when the infinite set of basis harmonics is truncated [Trampert and Snieder, 1996]. Hence it makes sense to conduct similar, independent studies that focus only on those continental areas that contain high levels of seismic activity and

<sup>1</sup>Now at Schlumberger Cambridge Research, Cambridge, England.

Copyright 1998 by the American Geophysical Union.

Paper number 98JB00903.  
0148-0227/98/98JB-00903\$09.00

station density. Using regional station arrays in addition to GDSN data, we thus focus on areas which are traversed by the highest density of short paths. In such areas it is possible to increase the resolution beyond that attainable in current global models.

Many such studies have been pursued using local to regional scale data within or off the coast of Eurasia, e.g., using body waves, *Grand and Helmberger [1985]*, *Lyon-Caen [1986]*, *Zhao et al. [1991, 1992]*, *Spakman et al. [1993]*, *van der Hilst et al. [1993]*, and *Roecker et al. [1993]*; using surface waves, *Pines et al. [1980]*, *Romanowicz [1982]*, *Brandon and Romanowicz [1986]*, *Bourjot and Romanowicz [1992]*, *Curtis and Woodhouse [1997]*, and *Ritzwoller and Levshin [1998]*; and using waveform inversion, *Zielhuis and Nolet [1994]*, *Marquering and Snieder [1996]*, and *Muyzert and Snieder [1998]*. However, body wave studies generally only sample lithospheric structure in areas of high seismicity or dense receiver coverage since most ray paths dip steeply into the mantle, and most of the surface wave or waveform inversion studies have been limited in lateral extent and hence generally do not show how structures in one tectonic region link to those in another. One exception to this is the study of *Ritzwoller and Levshin [1998]*, who used manually measured fundamental mode surface wave group velocities for earthquake-station paths crossing most of Eurasia to construct Eurasian group velocity maps.

In this study we automatically analyzed over 32,000 vertical and horizontal component surface wave signals

and obtained reliable event-station fundamental mode phase velocity measurements from 4020 Rayleigh and 4389 Love waves traversing (assumed) great circle paths across the Eurasian continent. To do this, we used the technique of *Trampert and Woodhouse [1995]*, retuned to increase its effectiveness along shorter paths through more heterogeneous continental media. Measured phase velocities were then linearly inverted into phase velocity perturbations at each point across Eurasia.

This study fills a gap in the knowledge accrued in the references listed above: the resolution attained here is higher than that in previous global studies, and we span most of Eurasia and hence image regions linking tectonic zones rather than only the seismically active zones themselves. In addition, the fully automatic procedures used here allow a single operator to process a huge quantity of data very efficiently.

We also show that the particular sensitivity of the fundamental mode Rayleigh waves to shear velocity structure allows a new type of resolution test to be performed. All of the above studies use fully linearized tests to quantify resolution. In a similar manner we perform checkerboard style resolution tests which suggest that velocity anomalies with diameter  $\sim 750$  km and greater can be imaged across most of Eurasia, and contrasts with diameter  $\sim 500$ – $600$  km can be imaged across much of central and southeast Asia. However, these tests do not account for true data noise, errors in earthquake source parameters or deviations from our linearizing assumptions (e.g., no off-great circle path

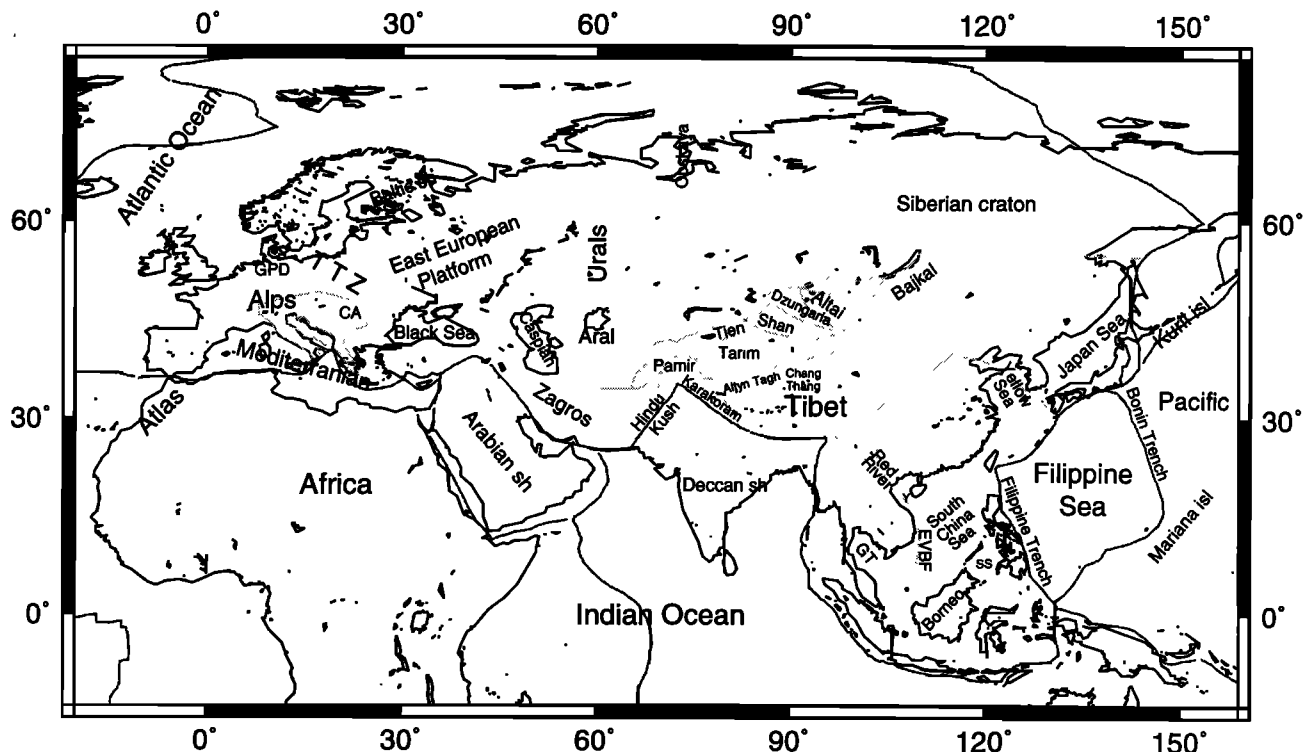


**Figure 1.** Geographical names used in the text. Abbreviations used are as follows: TTZ, Tornquist Teyzair zone; GPD, German-Polish depression; CA, Carpathian arc; GT, gulf of Thailand; EVBF, East Vietnam Boundary fault; SS, Sulu Sea; Y, Yinggehai basin (SE of Red River fault); sh, shield.

deviation). A different test of resolution which takes account of all of these effects is the correlation between the phase velocity maps and known tectonic or topographic features. For instance, actively deforming structures such as the Tibetan plateau separated from the Tien Shan mountains by the Tarim basin, regions of back arc extension in the Japanese Sea, the Zagros and Caucasus mountains, Turkey and the Aegean region are all areas of anomalous crustal thickness (many geographical locations mentioned in the text are shown in Figure 1). The Love wave phase velocity around 40 s period is extremely sensitive to Moho depth, and by assuming that the average crustal thickness at long wavelengths is isostatically increased where topography is highest we assess lateral resolution by comparing Love 40 s phase velocity with topography. All of the regions listed above are resolved confirming a significant improvement over global models.

Finally, again owing to the particular nature of the Rayleigh fundamental mode sensitivity kernels, we show that the phase velocities can be interpreted directly in terms of shear velocity using a phase velocity slicing technique. This constitutes a new tool for use in phase velocity studies, and in this case it illuminates dipping subduction zones and areas of back arc extension as high- and low-velocity features, respectively, the first time that dipping slabs have been imaged in large scale fundamental mode phase velocity studies.

The above results attest to the respectable lateral resolution of each phase velocity map individually and visually show the correlation of all periods together in the case of phase velocity slices. R. Devilee et al. (Using neural networks to invert surface wave dispersion data for crustal thickness across Eurasia, submitted to *Journal of Geophysical Research*, 1998, hereinafter referred to as Devilee et al., submitted manuscript) show that the information contained in the entire data set across periods 30s–100s is robust by using neural networks to interrogate these phase velocities for crustal thickness variations across Eurasia [see also Curtis et al., 1997]. To within the limitations of depth resolution imposed by using phase velocity data alone, the results agree with those predicted in the global a priori model of the lithosphere proposed by Mooney et al. [1998], confirming that the various phase velocity maps are mutually consistent.

## 2. Methodology

Phase velocities in the period range 20–170 s were extracted from surface wave trains using the automatic technique developed by Trampert and Woodhouse [1995]. The theory will be summarized here for completeness and so that we can describe our deviations from the original algorithm; we refer you to the original paper for a detailed discussion of the method's robustness. The complete methodology from data filtering and selection through to final inversion for local phase velocity perturbations is summarized in Figure 2.

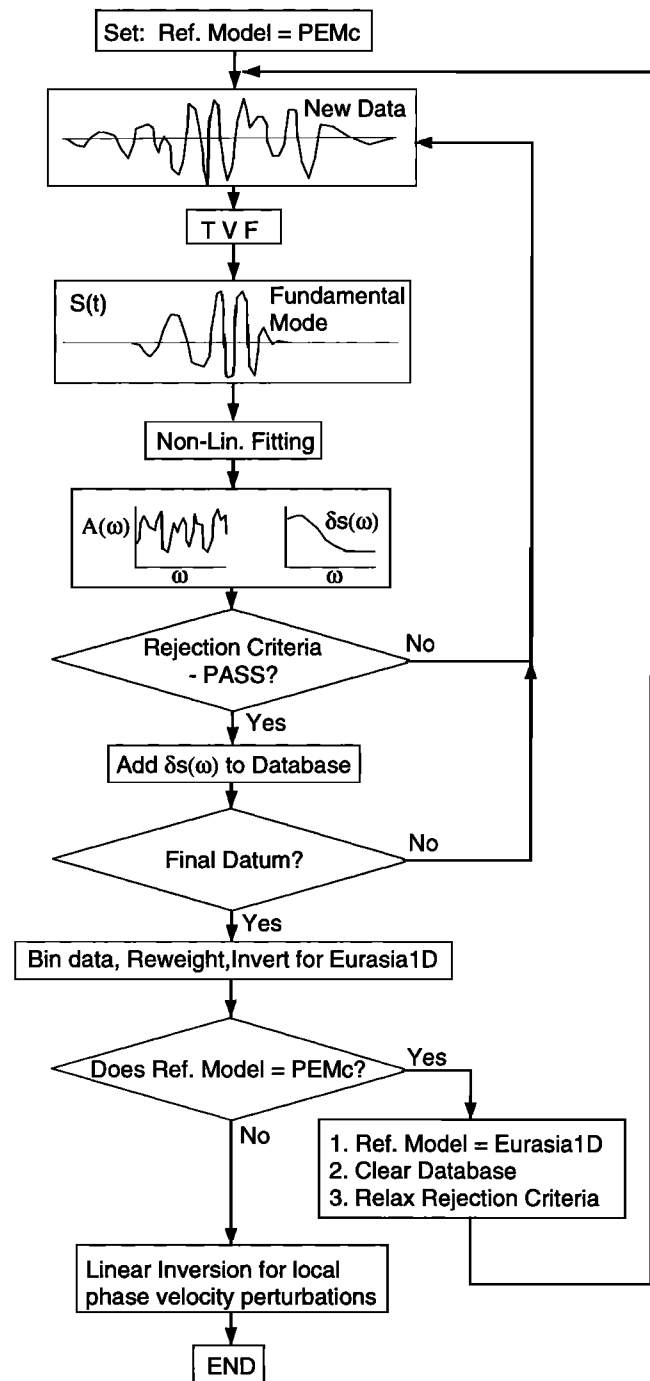


**Figure 2.** Flow chart of the data processing and inversion cycle used in the current work. See section 2 for details. TVF, time variable filtration; PEMc, continental preliminary Earth model [Dziewonski et al., 1975].

### 2.1. Data Selection and Phase Velocity Measurement

We initially selected waveforms for which the earthquake and station lay within longitude range 40°W to 180°E, latitude range 40°S to 90°N, with earthquake magnitude  $M_w > 5.2$ , and epicentral distance in the range 20°–160° (to avoid near-source effects and interference with the R2 arrival). The data comprised all

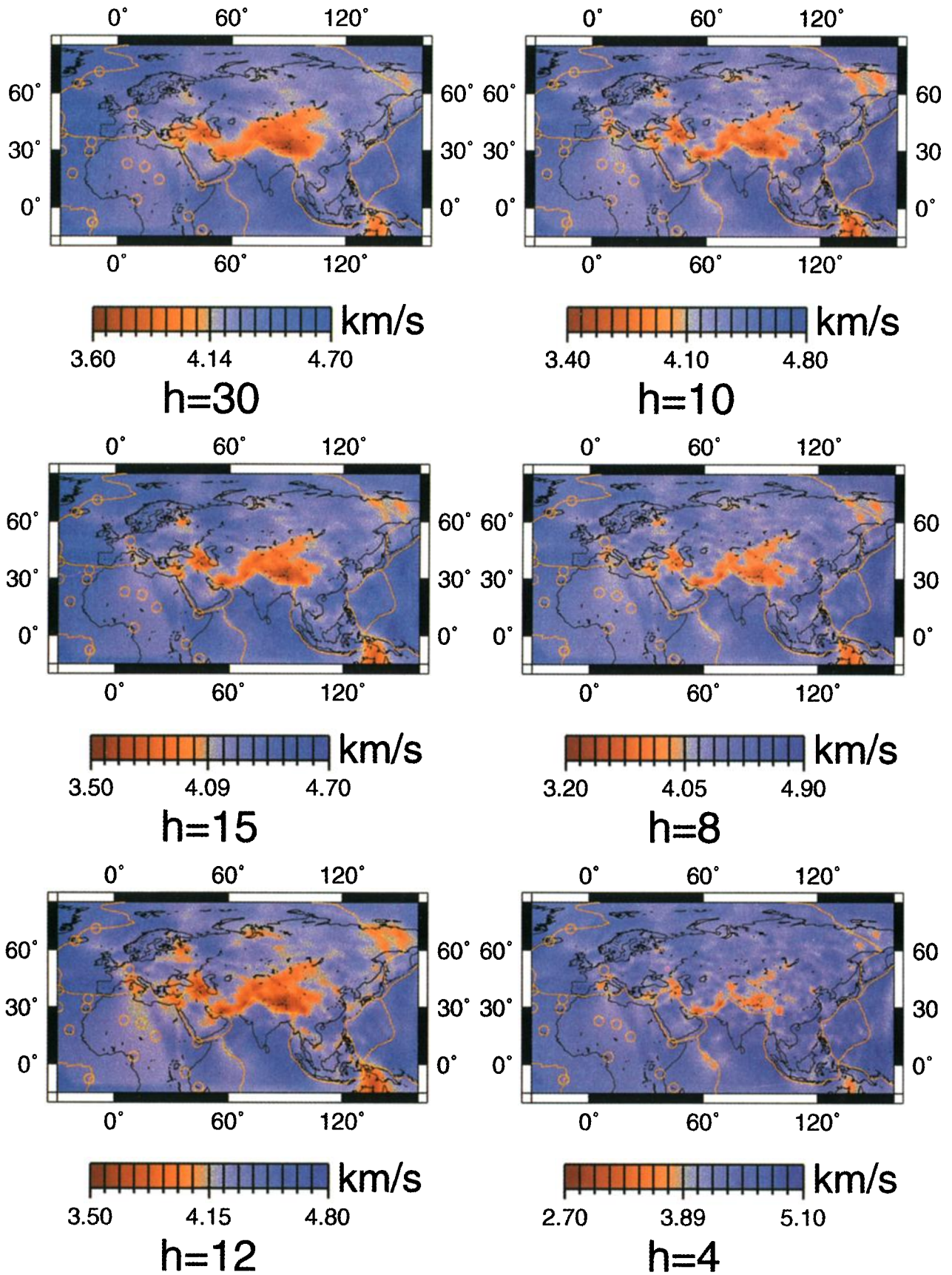


Plate 1. Love wave 40 s fundamental mode phase velocity models for various values of first derivative damping parameter  $h$  (in equations (13)–(15)).

available IRIS GDSN (Incorporated Research Institutions for Seismology Global Digital Seismograph Network) and Geoscope data for the period 1979 to 1996, NARS (Network of Autonomously Recording Seismographs) data from 1980–1995, plus some regional stations included in the SPYDER network (see, e.g., *Morelli* [1994] for a review). In total, we selected 33,192 vertical and 32,404 transverse component seismograms which record Rayleigh and Love surface waves, respectively.

Each recorded seismogram was time variable filtered around the fundamental mode surface wave group arrival predicted by continental Preliminary Earth Model PEMc [*Dziewonski et al.*, 1975] using the group velocity envelopes defined by *Cara* [1973] to extract the fundamental mode portion of the signal [*Landisman et al.*, 1969]. We may then write the observed seismogram in terms of an amplitude and phase perturbation to a synthetic seismogram containing fundamental mode surface waves propagated through PEMc:

$$D(\omega) = A(\omega) \exp[i\omega\Delta \delta s(\omega)]S(\omega) \quad (1)$$

Here  $\Delta$  is the epicentral distance,  $A(\omega)$  is the amplitude scaling factor, and  $\delta s(\omega)$  is the phase perturbation required to make the synthetic signal  $S(\omega)$  match the filtered data signal  $D(\omega)$ , where  $\omega$  is angular frequency. Equation (1) may be broken into two parts, for amplitude and phase, respectively. For amplitude we obtain

$$|D| = A |S| \quad (2)$$

and for phase we obtain two coupled equations:

$$D_r = A[S_r \cos(\omega\Delta\delta s) + S_i \sin(\omega\Delta\delta s)] \quad (3)$$

$$D_i = A[S_i \cos(\omega\Delta\delta s) - S_r \sin(\omega\Delta\delta s)] \quad (4)$$

where subscripts  $r$  and  $i$  stand for real and imaginary components and where we have dropped the  $\omega$  dependence for notational convenience. We parameterize the amplitude perturbation  $A(\omega)$  and phase velocity perturbation  $\delta s(\omega)$  in terms of cubic B splines [e.g., *Lancaster and Salkauskas*, 1986]. Hence equation (2) poses a linear inverse problem for spline coefficients of  $A(\omega)$ , while equations (3) and (4) define a nonlinear inverse problem for the coefficients of  $\delta s(\omega)$ .

The linear inverse problem for amplitude  $A(\omega)$  may be solved immediately using standard linear least squares algorithms [*Tarantola and Valette*, 1982]. The solution to the nonlinear inverse problem is found by iterated linearized inversions, and hence is dependent on the starting model used for the phase slowness perturbation  $\delta s(\omega)$ . This is constructed as follows: for each seismogram we estimate the fundamental mode group velocity  $u(\omega)$  by measuring the frequency-dependent maximum group amplitude of the analytically extended (time variable filtered) seismogram, i.e., with imaginary extension equal to the Hilbert transform of the real seismogram [*Dziewonski et al.*, 1969]. By using the analytic relationship between group and phase velocity  $c(\omega)$ ,

$$u(\omega) = \frac{c(\omega)}{1 - \frac{\omega}{c(\omega)}c'(\omega)} \quad (5)$$

we calculate the phase slowness perturbation from PEMc corresponding to the measured group velocity perturbation  $\delta u(\omega)$ :

$$\delta u(\omega) = \delta s(\omega) + \omega\delta s'(\omega). \quad (6)$$

This constitutes a straightforward linear inverse problem for spline coefficients of  $\delta s(\omega)$  and hence provides the required initial estimate of phase slowness perturbation. During the subsequent nonlinear inversion of equations (3) and (4) we again apply the constraint that the phase velocity must be consistent with the measured group velocity (through equation (6)) with a relative weight  $10^{-5}$  compared to the phase data. Thus the group velocity is used as an additional, weak smoothing constraint which helps to stabilize the nonlinear inversion. Finally, we shift the whole phase spectrum by a constant number of cycles to best fit the phase velocity of PEMc at 150 s.

The inverse problems defined in equations (2) to (4) are solved by minimizing the cost function

$$\Phi_1(\mathbf{m}) = [\mathbf{d} - \mathbf{G}(\mathbf{m})]^T \mathbf{C}_d^{-1} [\mathbf{d} - \mathbf{G}(\mathbf{m})] + \mathbf{m}^T \mathbf{C}_m^{-1} \mathbf{m} \quad (7)$$

where model vector  $\mathbf{m}$  represents either  $A(\omega)$  (equation (2)) or  $\delta s(\omega)$  (equations (3) and (4)), vector  $\mathbf{d}$  represents the relevant left-hand side of equations (2) to (4),  $\mathbf{C}_d$  and  $\mathbf{C}_m$  are the expected data and model covariance matrices, and the forward operator  $\mathbf{G}$  relates the data  $\mathbf{d}$  to model  $\mathbf{m}$  by  $\mathbf{d} = \mathbf{G}(\mathbf{m})$ . The solution is given by single (linear case) or multiple (nonlinear case) iterations of

$$\mathbf{m}_{i+1} = \mathbf{m}_0 + (\mathbf{G}^T \mathbf{C}_d^{-1} \mathbf{G} + \mathbf{C}_m^{-1})^{-1} \times \mathbf{G}^T \mathbf{C}_d^{-1} [(\mathbf{d} - \mathbf{G}(\mathbf{m}_i)) + \mathbf{G}(\mathbf{m}_i - \mathbf{m}_0)] \quad (8)$$

Since phase dispersion curves are intrinsically smooth, we apply second derivative damping in our solution. This has two positive consequences: first, smoothness of the resulting slowness perturbations effectively resolves  $2\pi$  ambiguities in phase by smoothly interpolating between longer periods and shorter periods (this is identical to what an operator would do when measuring phase manually). Second, by applying the similar regularization in the amplitude inversion, the retrieved model for  $A(\omega)$  interpolates smoothly through notches in the amplitude spectrum. As described below, this is used to check for amplitude anomalies caused for instance by interfering multipathed arrivals, the receiver lying along a source nodal plane or indeed due to any other effect.

The smoothness constraint is applied by setting

$$\mathbf{C}_m^{-1} = p \cdot \mathbf{H} \quad (9)$$

where

$$H_{ij} = \int_{\omega_1}^{\omega_2} \frac{d^2 B_i(\omega)}{d\omega^2} \frac{d^2 B_j(\omega)}{d\omega^2} d\omega \quad (10)$$

with  $B_j(\omega)$  representing the  $j$ th B spline basis function of model  $\mathbf{m}$ , and  $[\omega_1, \omega_2]$  is the angular frequency range considered. The data covariance matrix  $\mathbf{C}_d$  is taken to be the identity matrix so that parameter  $p$  controls the trade-off between roughness and data fit. In the current implementations,  $p = 10^{-6}$  as used by *Trampert and Woodhouse* [1995, 1996], giving priority to data fit.

## 2.2. Error Detection, Data Rejection, and Uncertainty Estimates

Since phase velocities are measured automatically from each seismogram, some of the most important aspects of the measurement algorithm are the error detection and data rejection procedures. These are implemented as follows:

1. We define signal to be the fundamental mode surface wave and noise to be any energy arriving before the fundamental mode (including strong higher modes that may interfere with the fundamental signal). We define the respective portions of the signal using group velocity windows around PEMc, and reject data if the signal to noise ratio is less than 4. The group windows used are 5.4, 4.9, and 3.0 km/s for Love and 5.2, 4.4, and 2.4 km/s for Rayleigh waves, where the first two velocities in each case bound the “noise” and the second two bound the signal.

2. The retrieved amplitude model is smoothed by minimizing the roughness  $\mathbf{H}$  in equation (9). Thus the fitted amplitude  $A(\omega)|S(\omega)|$  interpolates through notches in the signal amplitude spectrum where the signal phase may become effectively undefined. Hence notches may be detected by comparing the true amplitude at each frequency with  $A(\omega)$ . We reject all signals for which the amplitude variance reduction is less than 95% and those for which the minimum value of  $A(\omega)$  is  $<0.1$  for any  $\omega$  in the frequency range measured.

3. Signals for which the measured relative group velocity perturbation  $\delta u(\omega)/u^R$  is  $>15\%$ , where  $u^R$  is the group velocity of PEMc, are rejected.

4. To effectively remove problems of cycle skipping as we trace the signal phase from high periods to low periods, we reject all signals which have  $<95\%$  variance reduction in the nonlinear inversion for  $\delta c(\omega)$ , or which have a maximum relative phase velocity perturbation  $\delta c(\omega)/c^R$  greater than 15%, where  $c^R$  is the phase velocity of PEMc.

The variance reduction threshold in the amplitude and phase fit was increased from 85% in the study of *Trampert and Woodhouse* [1995, 1996] to 95% in this study. We believe this is necessary to detect the interference of both multipathed arrivals and of higher modes with the direct fundamental mode signal. These sources of noise are strongly correlated both temporally and spatially, and hence the number of “infected” seismograms in our data set must be reduced to a minimum. This extremely conservative threshold is used to collect an initial data set with which we construct a

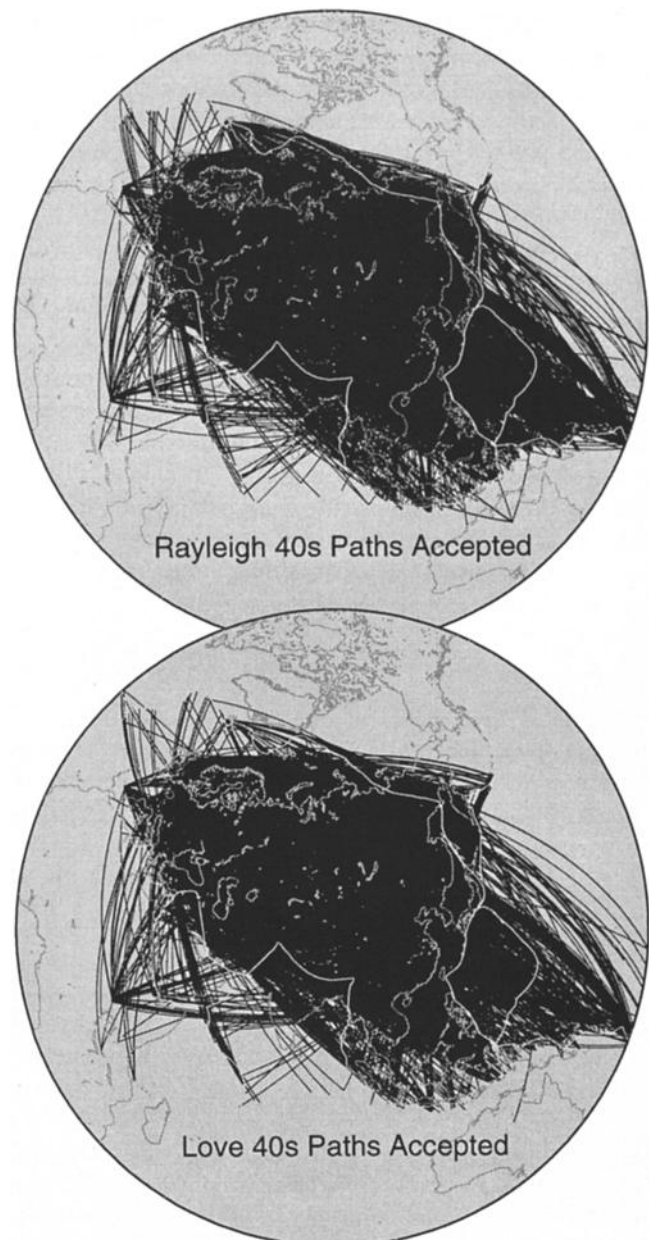


**Figure 3.** Great circle paths along which average phase velocities were measured at all periods between 26 s and 150 s period. These were used to construct the one-dimensional velocity model Eurasia1D.

one-dimensional model of the phase velocity structure across Eurasia (see below). The threshold will be relaxed slightly in a later stage of processing.

Note that data are rejected if any of the quality control criteria are contravened at any frequency. Since multipathed arrivals and associated phase disturbances are likely to be maximum at low periods, we could have created different data sets which satisfy all quality controls within certain period ranges (e.g., one data set which is of good quality in the period range 170–20 s, and a residual data set which is of good quality in the range 170–45 s as done by *Ekström et al.* [1997]),

or we could accept arbitrary period ranges with robust measurements for each signal individually as done by *van Heijst and Woodhouse* [1998] for phase velocities and *Ritzwoller and Levshin* [1998] for group velocities. However, our aim is to collate a data set with roughly homogenous information content at all periods. Phase velocity maps may then be created which are approximately equally well-resolved at each period and hence which are as mutually consistent as possible (under our linearized assumptions). Thus subsequent point-wise inversions of phase velocity for shear velocity structure with depth become meaningful. For these reasons we did not follow either of these options, instead accepting less abundant data for the sake of consistency.

The initial data set consists of measurements of 2955 Rayleigh and 3627 Love wave  $dc/c^R$  (omitting the  $\omega$  dependence for convenience), and the corresponding great circle paths are shown in Figure 3. Most of Eurasia is covered, and the data set contains considerable redundancy since many paths are approximately repeated. We use this redundancy to obtain estimates of data uncertainty by checking measurement repeatability on independent but geographically similar paths as follows. First, the geographic area is divided into cells of  $2.5^\circ \times 2.5^\circ$ . Paths with robust measurements are binned into sets which have end points within common cells. For each bin with eight paths or more, the frequency-dependent phase velocity variance is calculated, and these variances are assigned to each phase velocity measurement within that bin. The global average frequency-dependent variance over all such bins is calculated, and this is assigned to all paths which lie in bins containing less than eight paths. The value eight was chosen as a safe threshold because for values of five or less, bins occasionally occurred (by chance) which had artificially low variances at some frequency due to the small number of samples used in the estimate. These paths dominate the inversion for phase velocity maps and appear as streaks in the final plots. This artifact did not appear for threshold values greater than five.

We then construct a one-dimensional model of phase velocity for the area under study by taking the average of all measured relative phase velocity perturbations  $dc_i/c^R$ , weighted by the inverse of their respective variances  $\sigma_i^2$  and by the number of paths  $n_i$  in the bin to which path  $i$  belongs:

$$\frac{\overline{dc}}{c^R} = \frac{\sum_{i=1}^N \left[ \frac{dc_i}{c^R} \times \frac{1}{n_i \sigma_i^2} \right]}{\sum_{i=1}^N \frac{1}{n_i \sigma_i^2}} \quad (11)$$

Downweighting by the factor  $n_i$  makes this procedure approximately equivalent to using summary rays between each pair of cells by avoiding extra weight being given to geographical locations traversed by many almost identical paths.

The resulting phase velocity model is called Eurasia1D and is shown in Figure 4a. In addition, we converted the phase velocity curves to group velocity using equation (5) and these are shown in Figure 4b. In Figures 4a and 4b the corresponding velocities of the preliminary reference Earth model (PREM) [Dziewonski and Anderson, 1981] are shown for reference and the phase velocities of PEMc, and average group velocities obtained by *Ritzwoller and Levshin* [1998] over a similar geographical area are also shown. Eurasia1D phase velocities are lower than the continental reference model at all periods but converge toward it both at long ( $>140$  s) and short ( $<40$  s) periods. Eurasia1D group velocities match the average group velocities found by *Ritzwoller and Levshin* to within 0.1 km/s at all periods, although Eurasia1D is consistently slightly slower. They measured group velocity directly using a manual method, and hence this slight discrepancy between

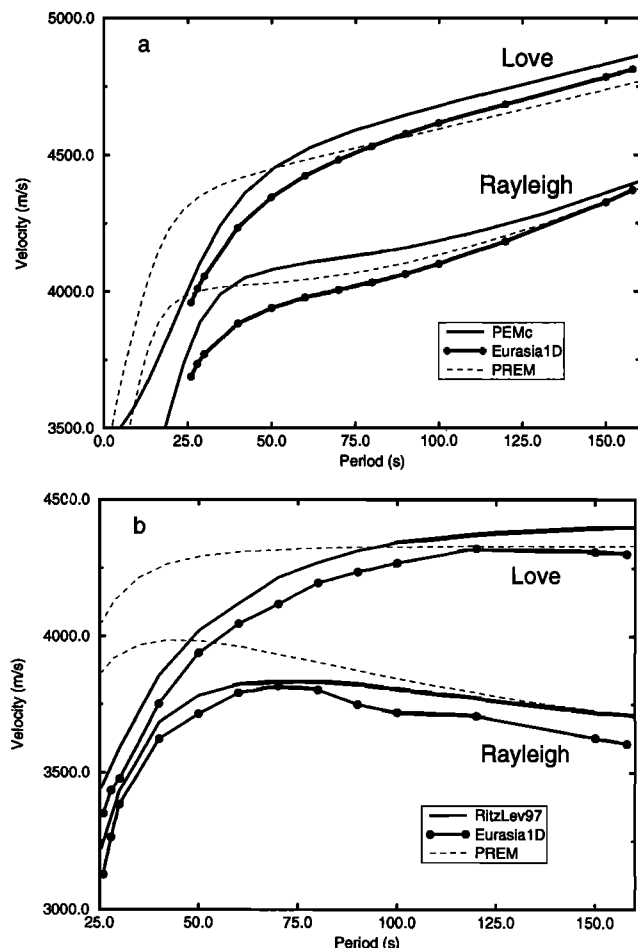


**Figure 4.** The one-dimensional velocity model Eurasia1D: (a) phase velocities and (b) group velocities. In Figure 4a the corresponding phase velocities for reference Earth model PREM and continental model PEMc are also shown [Dziewonski et al., 1975; Dziewonski and Anderson, 1981]; in Figure 4b the group velocities for PREM and the average model from *Ritzwoller and Levshin* [1998] are shown.

the two studies could be imposed by their operators who manually grade each group velocity measurement or by our automated data selection procedures. However, the overall consistency between the two results makes it highly unlikely that more than 0.1 km/s of absolute bias exists in either study.

Finally, we construct a new data set, with the same type of rejection criteria as before, but this time with the maximum relative group and phase velocity deviations  $\delta c(\omega)/c^R$  and  $\delta u(\omega)/u^R$  in criteria 3 and 4 above, respectively, redefined to be relative perturbations with respect to Eurasia1D instead of PEMc. In addition, since we include data from relatively short paths which may traverse predominantly oceanic areas on the Eurasian margins (e.g., the Philippine sea), we extend the a priori acceptable level of heterogeneity and accept up to 15% negative deviations, 15% positive deviations for periods  $>70$  s, and up to 22% positive deviations for periods  $<70$  s in both group and phase velocity. At periods  $<70$  s this criterion allows the large positive deviations from Eurasia1D expected from Figures 4a and 4b (PREM) for mixed oceanic-continent paths. We also relax the variance reduction threshold in criteria 2 and 4 to 85%. By reselecting the data in this way we hope to diminish any biases in our data set due to our choice of initial reference model PEMc which, as has just been shown, is slightly too fast for Eurasia at all periods considered. Using the reselected data, we also recalculated a one-dimensional average phase velocity model in the same way as above and found that it was almost identical to Eurasia1D; hence our initial estimate of Eurasia1D was not biased. The final data set consists of 4020 Rayleigh and 4389 Love wave fundamental mode phase velocities along great circle paths distributed very similarly to those shown in Figure 3.

### 2.3. Creating Phase Velocity Maps

Relative phase velocities on all paths at periods 26, 30, 35, 40, 45, 50, 60, 70, 80, 90, 100, 115, 130, and 150 s were inverted for phase velocities in each cell of a gridded triangular cell geometry. This process constitutes a standard linear inverse problem,  $\mathbf{d} = \mathbf{G}\mathbf{m}$ , where now  $\mathbf{d}$  is the vector of measured relative phase velocities  $dc/c^R$  along each path at a fixed frequency,  $\mathbf{m}$  is the model vector of relative phase velocities in each gridded cell, and  $\mathbf{G}$  is the matrix of partial derivatives with elements  $G_{ij} = \delta d_i / \delta m_j$  equal to length of path  $i$  in cell  $j$  divided by total length of path  $i$ , where we assume great circle paths between source and receiver. We find the least squares solution by minimizing the cost function

$$\Phi_2(\mathbf{m}) = [\mathbf{d} - \mathbf{G}(\mathbf{m})]^T \mathbf{C}_d^{-1} [\mathbf{d} - \mathbf{G}(\mathbf{m})] + (\mathbf{D}\mathbf{m})^T (\mathbf{D}\mathbf{m}) \quad (12)$$

using the gradient descent method of *Paige and Saunders* [1982]. Here  $\mathbf{D}$  is a first derivative damping matrix with elements

$$D_{ij} = h \quad (13)$$

if cells  $i$  and  $j$  are neighboring,  $i > j$ ,

$$D_{ij} = -h \quad (14)$$

if cells  $i$  and  $j$  are neighboring,  $i < j$ , and

$$D_{ij} = 0 \text{ otherwise} \quad (15)$$

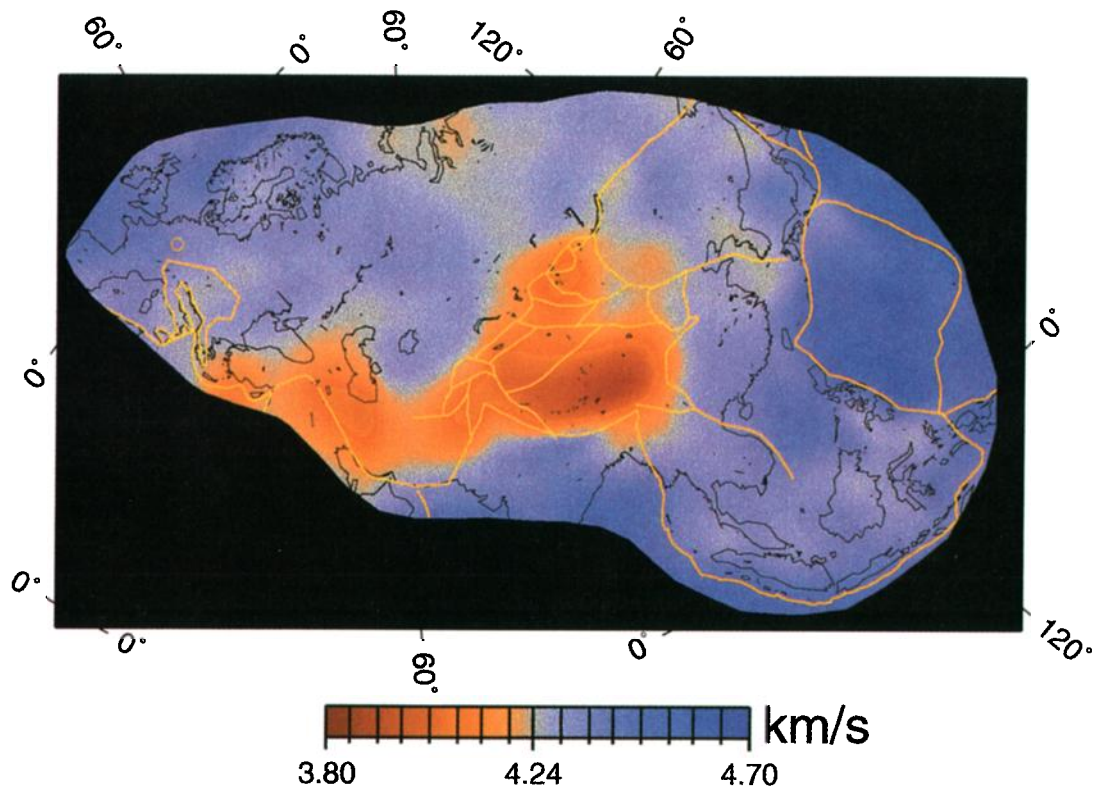
where neighboring cells are defined to be those which share a common boundary. By minimizing  $\Phi_2$  we attempt to satisfy  $\mathbf{D}\mathbf{m} = \mathbf{0}$  with weight  $h$  with respect to the data fit, thereby finding the model with least cumulative horizontal gradient.

$\mathbf{C}_d$  is the data covariance matrix and is estimated as follows. First, we rebin the data and calculate variances in exactly the same way as before. We then multiply variances by the number of paths in the bin to which each path belongs (similar to equation (11)). The resulting variances constitute the diagonal elements of  $\mathbf{C}_d$ , and we arbitrarily set off-diagonal covariances to zero.

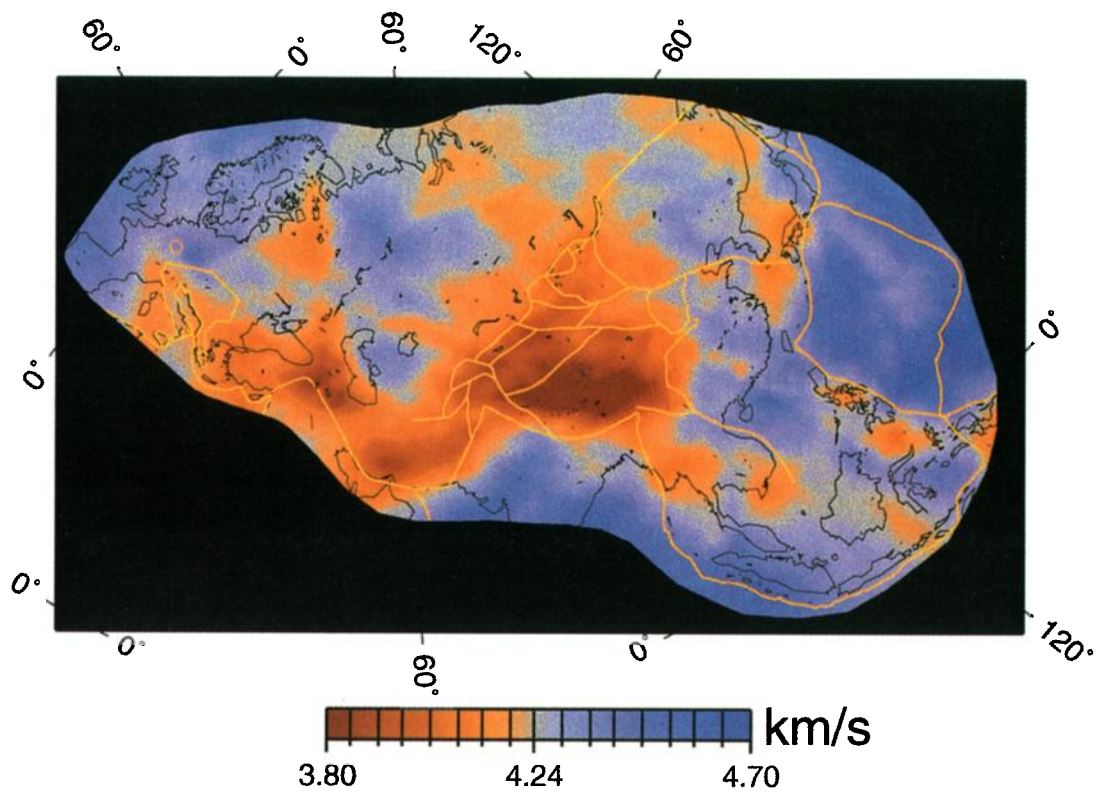
To avoid confusion, from here onward we refer to this process of creating maps from phase velocities as the "inversion" stage. We refer to the non-linear inversion for event-station average phase velocities from each individual seismogram described earlier as the phase velocity "measurement" stage.

### 3. First Derivative Damping, Data Weighting, and Resolution

We now explore the effects of varying the first derivative damping parameter  $h$  in equations (13) and (14), then we describe one final enhancement to our data weighting scheme, and last we analyze various measures of resolution in our final maps. Plate 1 shows maps of our Love wave phase velocity at 40s period for different values of  $h$ . When  $h = 30$ , a smoothed representation of the phase velocity structure is obtained. This map still represents the major velocity anomalies across Eurasia (the Tibetan plateau, Hindu Kush, Zagros and Caucasus mountains and the continent-ocean boundary), but details are lost due to the high degree of smoothing, and bias is introduced by damping major amplitude perturbations (e.g., the low Tibetan velocities are smeared across the Tarim basin, a huge Precambrian massif). At the opposite end of the spectrum,  $h = 4$  gives a model which is extremely rough. Major features like the Tibetan plateau and the Zagros mountains have all but disintegrated. This level of regularization is not sufficient to prevent noise in the data from being transferred into the model through the inverse system's null space and hence some intermediate value of  $h$  is desirable. We see from the other plots in Plate 1 that for values of  $h$  between 15 and 10, the pattern of anomalies becomes stable and only slight changes in amplitude occur. At  $h = 8$  the first signs of the instability evident when  $h = 4$  become apparent, and we assume that this is the point around which a significant portion of the data noise is mapped into our solution. Hence we



Ekstrom et al. Love 40s Phase Velocity



Curtis et al. Smooth Love 40s Phase Velocity

**Plate 2.** A comparison between our initial, smooth Love wave 40 s phase velocity model (using  $h = 30$ ) and the most recent global phase velocity model of *Ekström et al.* [1997]. Also, plate boundaries and tectonic boundary faults are shown in yellow [*Zonenshain and Savostin*, 1981; *Jackson and McKenzie*, 1984; *Zonenshain et al.*, 1990; *Lee and Lawver*, 1995].

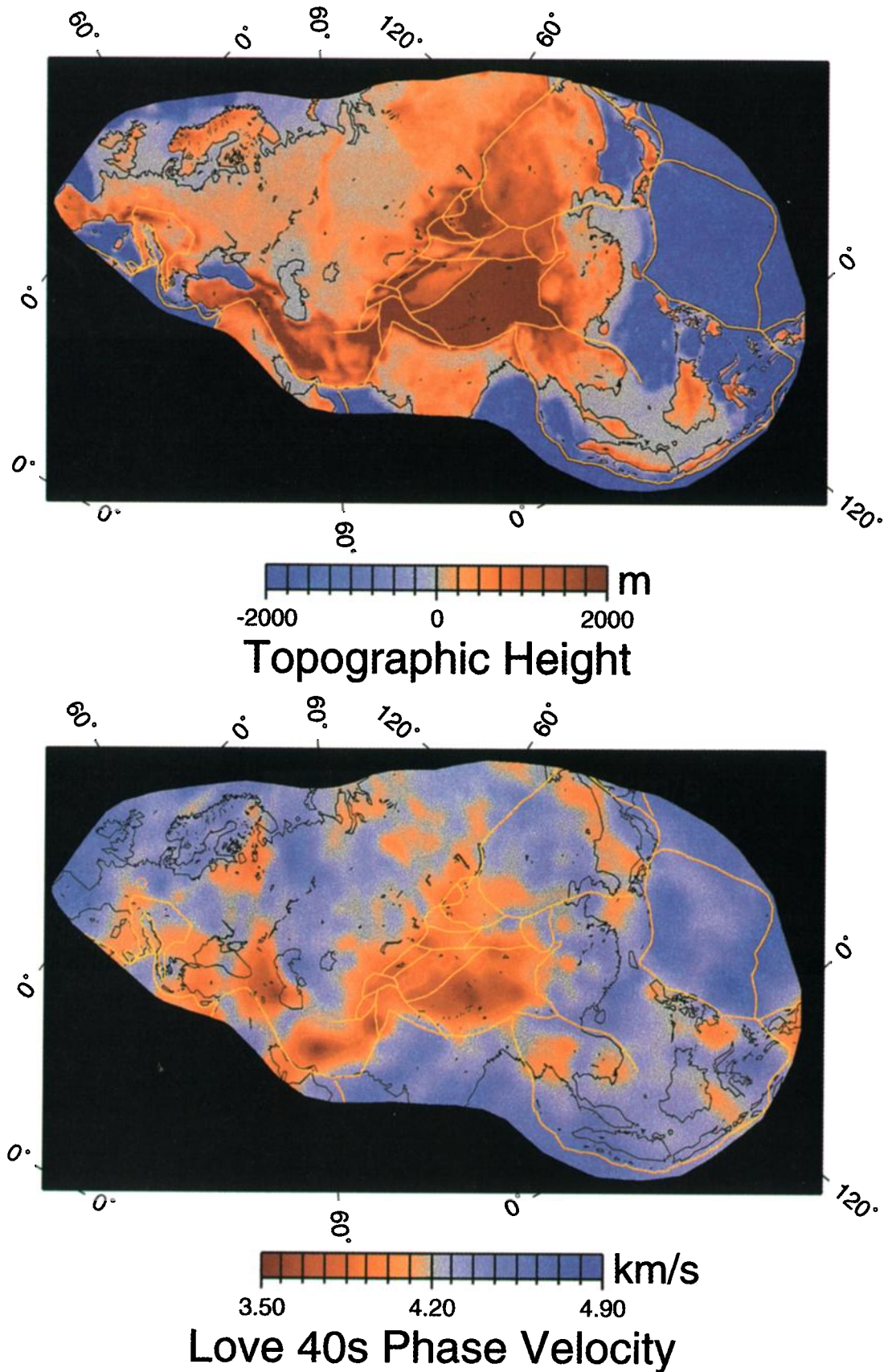


**Plate 3.** A comparison between our detailed Love wave 40 s period phase velocity map (using  $h = 12$ ) and topography. If isostasy holds at long wavelengths, then high topography should be balanced by thick crust, decreasing the average shear velocity in the lithospheric column. Hence Love 40 s phase velocity should be anticorrelated with topography. Tectonic boundaries shown are as in Plate 2.

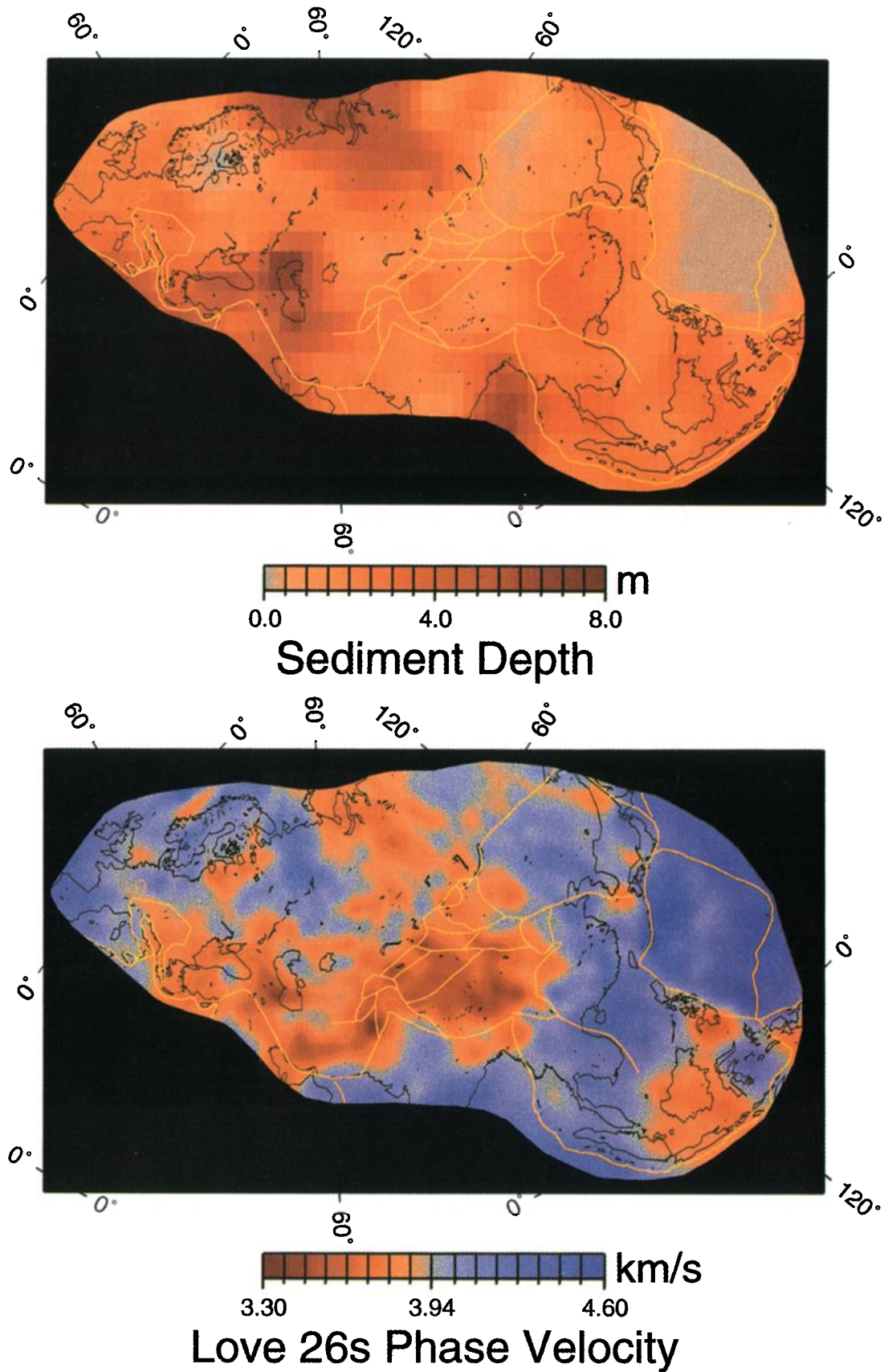


**Plate 4a.** Map of Love wave phase velocity at 26 s period with the total thickness of soft and hard sediments taken from the  $5^\circ \times 5^\circ$  global reference lithospheric model of *Mooney et al.*, [1998]. Tectonic boundaries shown are as in Plate 2.

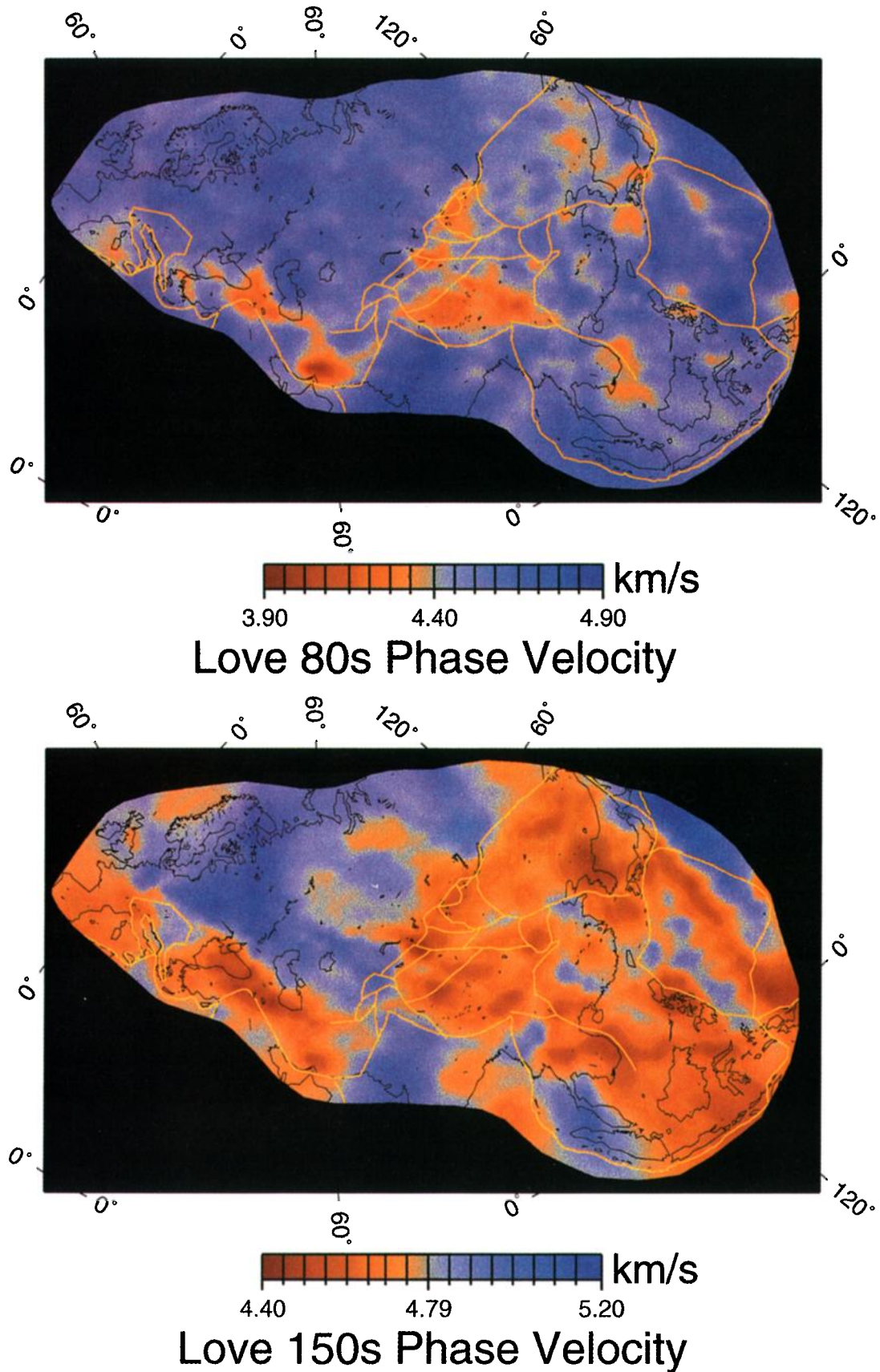


**Plate 4b.** Maps of Love wave phase velocities at 80 s and 150 s period. Tectonic boundaries shown are as in Plate 2.

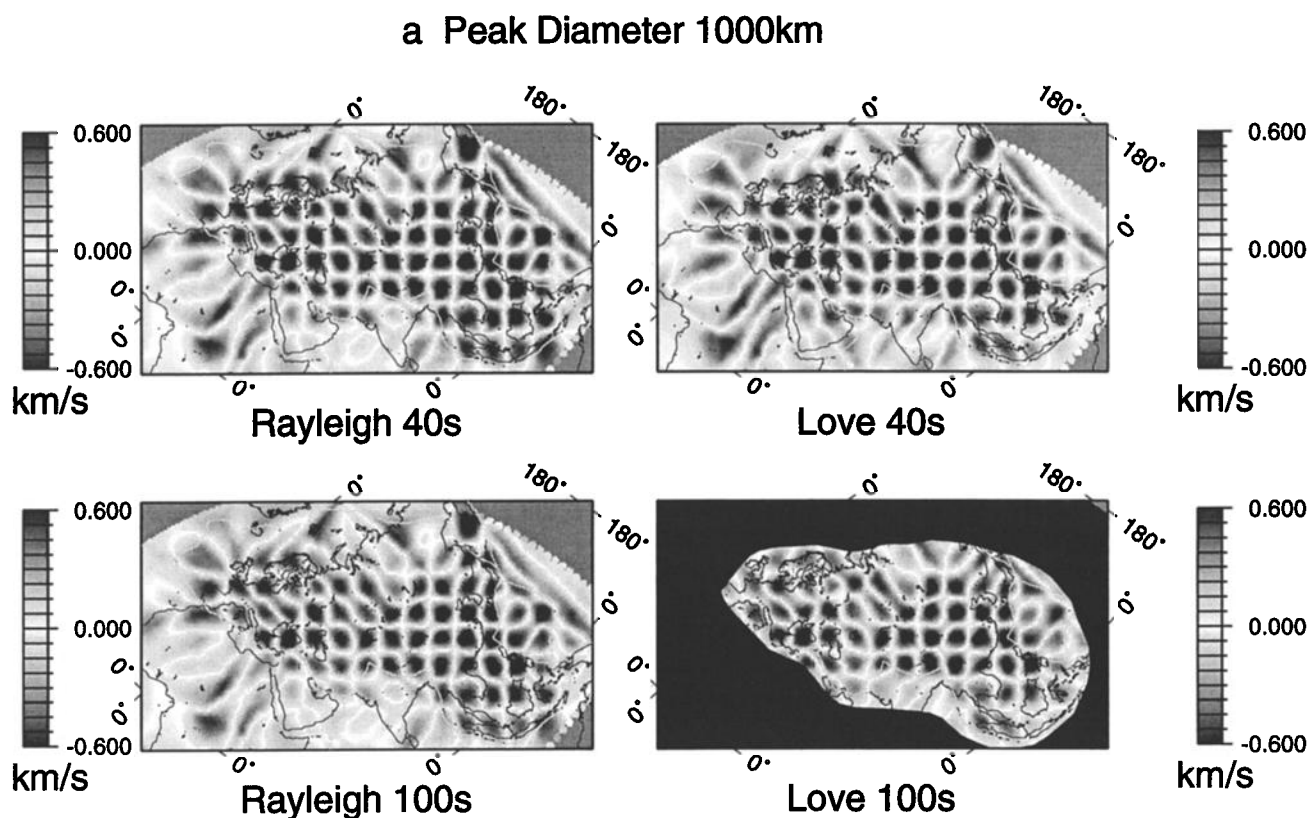


**Figure 5.** Checkerboard tests of resolution for Love and Rayleigh wave phase velocities for periods of 40 s and 100 s at peak diameters of (a) 1000 km, (b) 750 km, (d) 600 km and (e) 500 km. (c) For period of 150 s and peak diameters of 1000 and 750 km.

choose  $h = 12$  as representing a safe trade-off between data fit and model variance.

It is clear that for all values of  $h$ , noise in the data propagates into the phase velocity maps to some extent. Hence, at this stage it is crucial that all outlying data are removed (perhaps even at the expense of some good data), and we perform one further procedure of noise removal carried out for each period independently: first we invert for a very smooth map ( $h = 30$ ). Since most paths with robust measurements are fairly long, the data on almost all paths should be better fit by this smooth model. Hence we downweight by a factor of 2 all data for which the misfit reduction in this smooth inversion is  $<20\%$ .

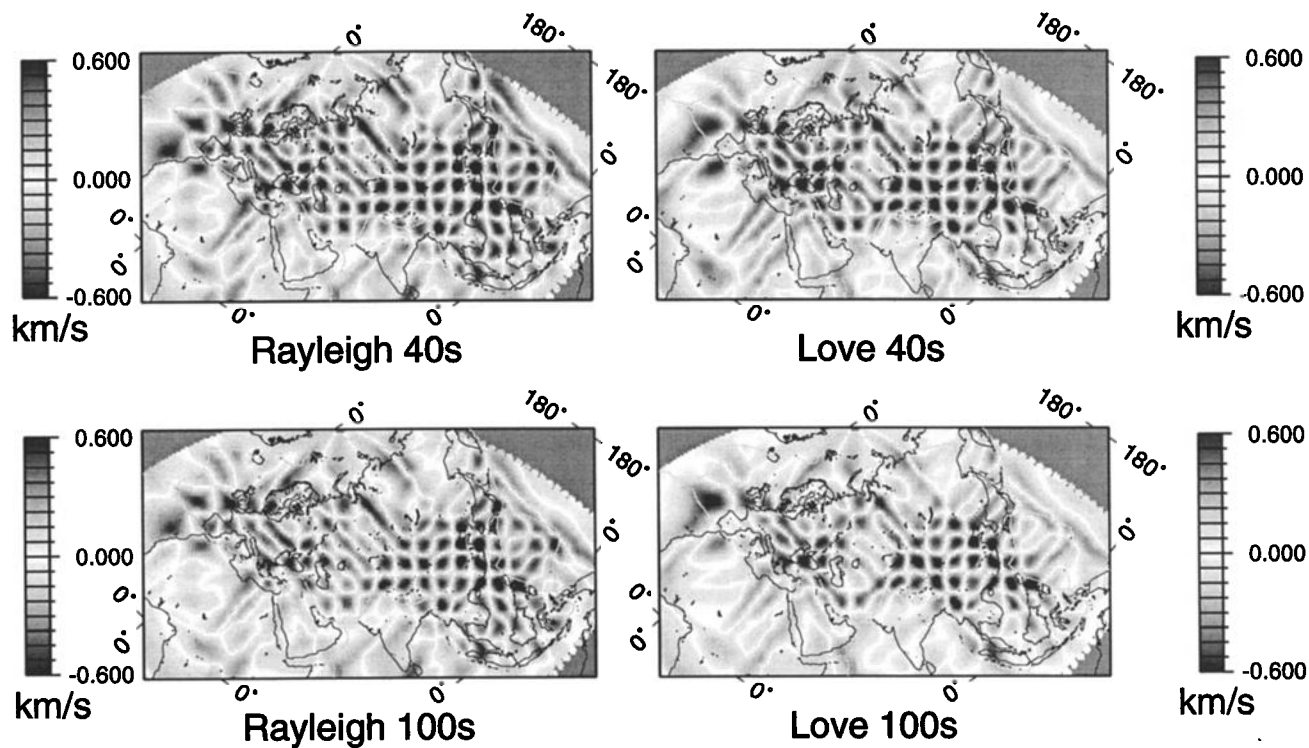
If any paths still contain anomalous data, then the effect of these will be suppressed by the large amount of robust data along neighboring paths due to smoothing. However, when we drop the smoothing parameter to allow very rough maps ( $h = 4$ ), the paths with anomalous data show up as streaks across the phase velocity maps. In this way we found 10 more Love and Rayleigh paths with outlying data and removed them from the database. Thus we produce the final data set and weighting system used to construct our detailed maps.

Plate 2 compares the smooth ( $h = 30$ ), initial phase velocity map of the 40 s Love wave with that of the most

recently published global phase velocity model of *Ekström et al.* [1997]. Although amplitudes vary between the models and the limited set of spherical harmonic basis functions and high degree of smoothing used by *Ekström et al.* ensure that no small-scale features enter their model, the pattern of anomalies in the maps are extremely similar within Eurasia. Hence this final stage of downweighting anomalous data is roughly equivalent to specifying that all data should be (at least slightly) better fit by the global heterogeneous models than by PEMc.

Figure 5 shows four checkerboard style tests using the updated weighting system and first derivative damping parameter ( $h = 12$ ). Sinusoidal input models with wavelengths 2000, 1500, 1200, and 1000 km giving peak diameters of 1000, 750, 600, and 500 km, respectively, are used to construct noise free synthetic travel times on all paths, and these were inverted using the true data weights. Hence, the plots in Figure 5 give an impression of the resolution limitations imposed by the path geometry in conjunction with the final data weighting system and level of regularization used. This can be thought of as the inherent resolution limits fixed by the problem formulation and level of data noise. The results suggest that features with diameter of the order of 1000–750 km should be resolved across much of mainland Eurasia and Indonesia. There is some smearing within central Rus-

**b Peak Diameter 750km**



**c Peak Diameter 750 - 1000km**

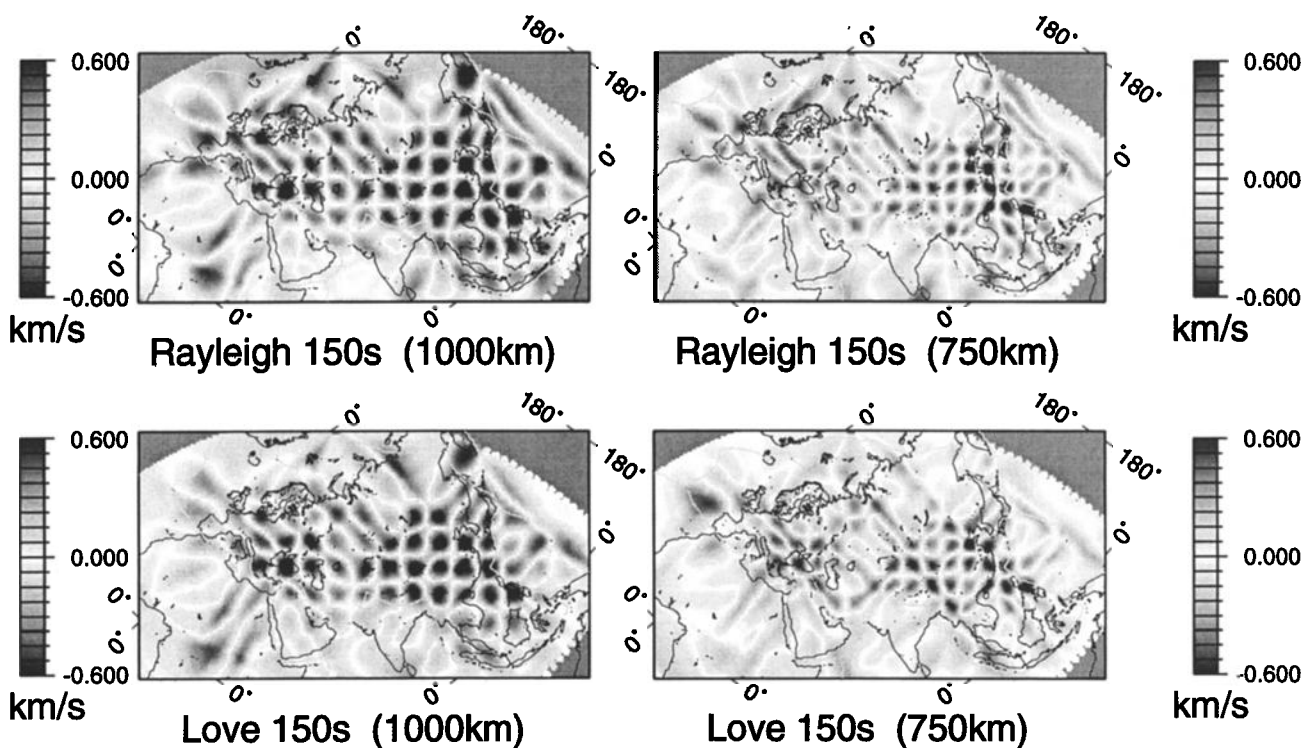
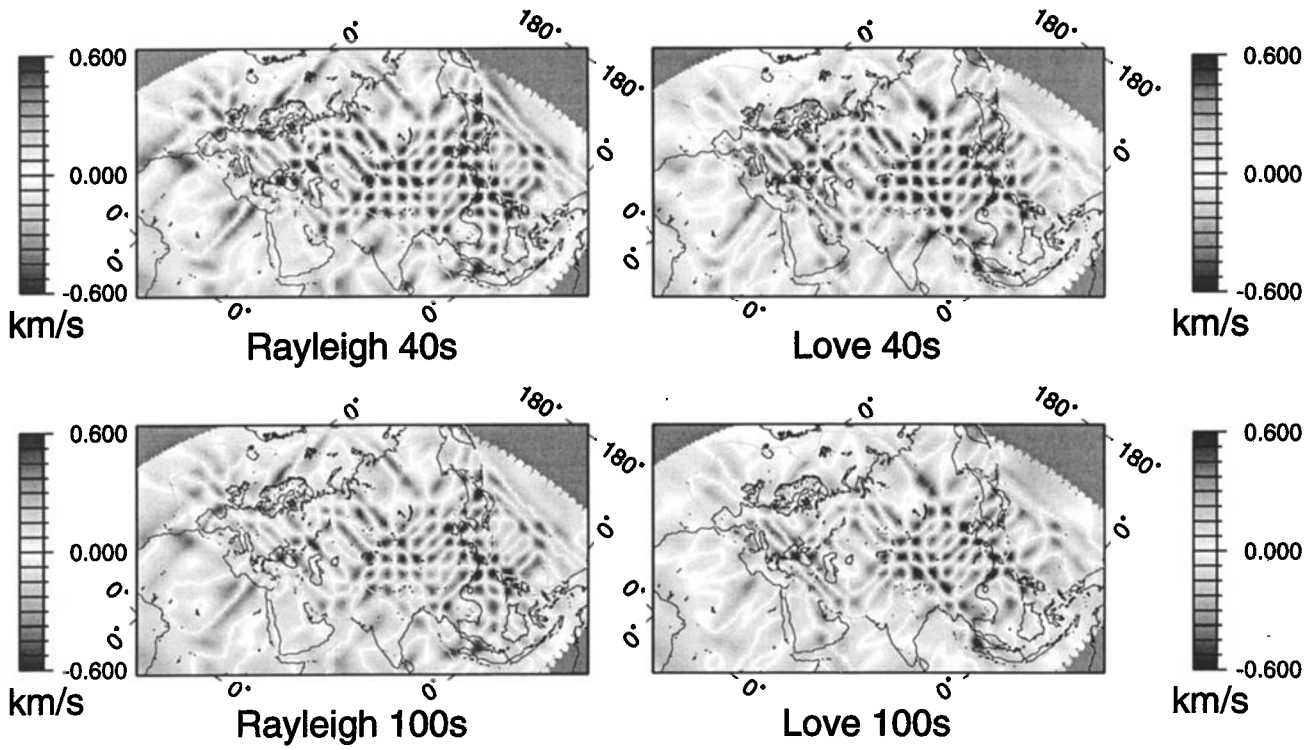


Figure 5. (continued)

**d Peak Diameter 600km**



**e Peak Diameter 500km**

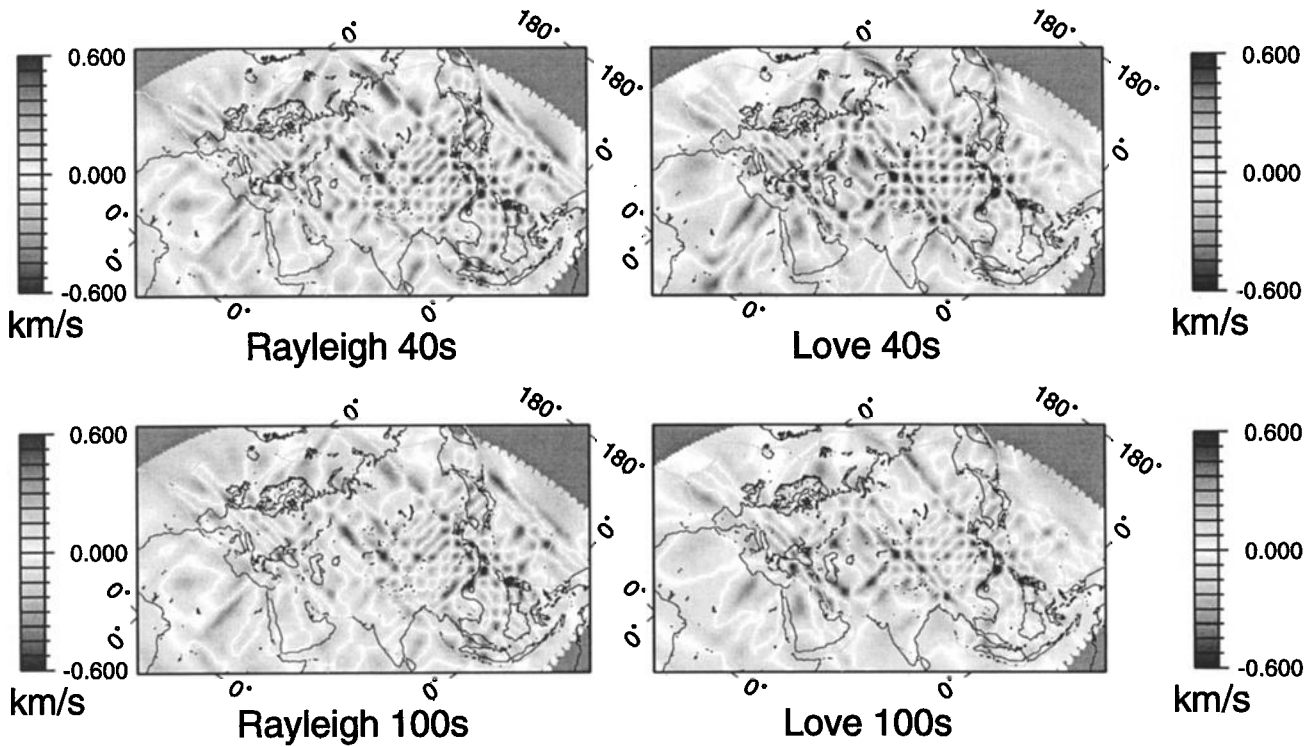
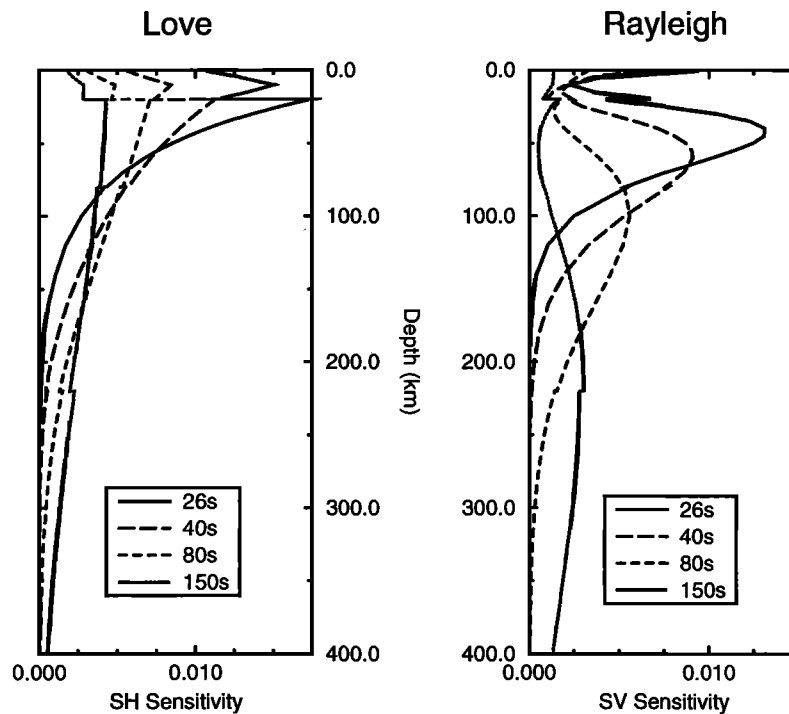


Figure 5. (continued)



**Figure 6.** Love and Rayleigh wave sensitivity with respect to horizontal and vertical shear velocity variations at depth, for periods of 26, 40, 80, and 150 s.

sia and NE Siberia is not resolved, but on the whole, the reconstruction is quite respectable. For diameters of around 600 km the lack of resolution in central Eurasia becomes more apparent, and for 500 km it becomes acute. Hence the reconstruction in western Eurasia appears to be limited to features of diameter around 750 km and greater apart from SE Europe which may be somewhat better resolved. However, across much of Asia the reconstruction is still very good even at diameters of 500 km, although the amplitude of the input model is diminished by around 50%. To focus attention on the areas in which at least 1000 km resolution is attained, we mask unresolved areas on all subsequent maps as shown in the final plot of Figure 5a.

Unless realistic data noise is added explicitly, checkerboard tests give only an indication of the resolution attainable given perfect (but weighted) data and if the assumptions inherent in the modeled physics hold true (e.g., great circle paths, double-couple earthquake sources, spatially varying anisotropy averages to zero in the isotropic inversion scheme). Another method to assess the true resolution of the retrieved models would be to compare them with some other physically measurable and completely independent quantity. Love wave 40 s period phase velocities are primarily sensitive to shear velocity  $V_s$  in the upper 100 km of the Earth with peak sensitivity around the Moho. The sensitivity kernel is positive and decreases to zero with increasing depth (Figure 6). Hence deviations in this phase velocity are approximately simple, weighted averages of

shear velocity anomalies in this depth range. One of the most significant contributions to such variations is due to crustal thickness heterogeneity; a thick crust has less high-velocity mantle material in the lithospheric column so that the average shear velocity is reduced. Hence the 40 s Love wave phase velocity map should be approximately anticorrelated with crustal thickness. If we assume that the larger scale features of the crustal thickness are (isostatically) positively correlated with increases in topographic height, then we expect a negative correlation between topography and phase velocity. This pattern will be perturbed primarily by strong variations in shear velocity in the upper lithosphere.

Plate 3 shows a comparison of topography and Love 40 s phase velocity. The observed correlation is striking in that even smaller scale features like the Tarim basin, Tien Shan, Hindu Kush, and Altai regions are fairly well correlated. These features can not be mutually distinguished on any of the current global phase velocity maps (e.g., see Plate 2), illustrating the greatly increased resolution that the current study offers. There are, however, areas where the correlation is poor. The most noticeable of these are the mountainous areas of Norway, the Urals, and the Iberian peninsula. The Urals are a narrow mountain belt and are certainly sub-resolution (Figure 5c). Resolution across the Iberian peninsula is poor due to low path coverage (Figures 3 and 5c). However, the poor correlation across Norway suggests either that resolution is poorer in this region than might be expected from the checkerboard tests or that signif-

icant positive shear velocity perturbations exist in the Norwegian lithosphere.

Both the checkerboard and the topography tests of resolution performed above are approximate. The checkerboard tests do not assess the direct effects of data errors or of unmodeled physics on resolution. Indeed, these are not true tests of resolution since no measure of trade-off between distinct model parameters is made. The correlation of Love wave 40 s phase velocity with topography takes into account all possible sources of error (including true model trade-offs, the effects of off-great circle path propagation, earthquake source errors, anisotropy, etc.). However, the true correlation between topography and phase velocity through crustal thickness is approximate due to nonisostatically compensated topography and to shear velocity variations. Moreover, the unmodeled physics will impose different errors on different periods of phase velocity, and there are no independent "target" data sets with which to correlate and compare measurements at longer periods or with Rayleigh waves. Hence, again this test only provides an impression of the lateral resolution attained.

However, from the tests above we estimate that features larger than 750 km in lateral extent should be resolved across most of Eurasia, apart from NE Siberia. In addition, across much of central and SE Asia, Indonesia and SE Europe, features larger than around 500–600 km may be resolved.

#### 4. Results

Plates 4 and 5 show the results of Love and Rayleigh wave phase velocity inversions respectively at periods of 26, 80, and 150 s, plus those for the 40 s Rayleigh wave (the 40 s Love wave phase velocities are shown in Plate 3). The inversions were performed on a grid of triangular cells with vertices 150 km apart, after which the maps were resampled at 30 km intervals for contouring. No subsequent smoothing or filtering has been performed.

Consider first the Love wave maps. As shown in Figure 6, Love waves are (primarily) sensitive to horizontal shear velocity variations with decreasing sensitivity with depth. For periods of 26 s, sensitivity is maximum between 0 and 50 km and is almost entirely confined to the upper 100 km of the Earth; as period increases, sensitivity extends to deeper levels until at 150 s period the phase velocity perturbation is an average of  $SH$  velocity anomalies over the upper ~300–400 km.

The Love 26 s phase velocity map in Plate 4a shows a first-order difference of around 0.6 km/s between the slow continents and fast oceans. Superimposed are variations most noticeably associated with mountain belts: the Tibetan plateau, Tien Shan, Hindu Kush, Caucasus, and Zagros. This association is at least partly due to crustal thickness variations as with the 40 s Love wave above. In addition, the 26 s data have suf-

ficiently shallow sensitivity that we also detect areas with thick sedimentary accumulations, especially the 1000 km-wide band of thick (~8 km) sediments that extend from Obshkaja gulf toward lake Baikal and a thinner band running from just north of Baikal toward the NE, the Tarim basin (~3 km), northern Japanese Sea (~4 km), southern Caspian Sea (~7 km), southern Black Sea (~7 km), and the eastern Mediterranean (~5 km), where all of the sediment depths are the combined thickness of soft and hard sediment in the model of *Mooney et al.* [1998] averaged across each region. The main basins which do not appear as low phase velocities on the map are the Ganges delta and the pre-Caspian depression just north and NW of the northern Caspian Sea. We do see low velocities across the sediment cover on the landward side of the Ganges delta, but the offshore area to the SE is oceanic so it is probable that the high shear velocities of the ocean lithosphere are swamping the low-velocity signal from the sediments. This may also be the case in the pre-Caspian depression which is also underlain by old oceanic lithosphere [*Zonenshain et al.*, 1990]. The latter basin was imaged by *Ritzwoller and Levshin* [1998] as an area of low Love 20 s group velocities, but these have a sensitivity kernel which is even more compressed toward the surface than the phase velocities used here and hence are less sensitive to the underlying lithospheric structure.

The correlations with topography and sediment cover observed in Plate 4a exist despite the fact that ray paths must deviate significantly from the great circle for this low period. Such deviations are a serious issue since they affect both anomaly locations and amplitudes. Including such effects in the forward modeling procedure may sharpen the image considerably.

As with the 40 s Love velocity in Plate 3, the 80 s Love velocity shows low-velocity features which are mainly associated with the mountain belts mentioned above, although additional low-velocity features exist in Indonesia, south of Japan, and on the continental border of the Japanese Sea. Between the 80 and 150 s periods, these low-velocity features become more pronounced, the low velocities across the Caucasus and Zagros merge to form a continuous feature which also extends into the Turkey–Aegean deformation system, and the low-velocity features in Tibet, Tien Shan, and Altai regions merge and extend to form a semi-continuous low-velocity zone which spans the whole of the Tibet–Mongolian mountain system of southeast Asia. Notice how this latter feature is approximately bounded by the outermost tectonic deformation boundaries shown on the map [*Zonenshain and Savostin*, 1981; *Jackson and McKenzie*, 1984; *Zonenshain et al.*, 1990; *Lee and Lawver*, 1995] and that at 150 s period the peak low velocities are not all beneath areas with the highest average topography. Since the 40 s Love wave did not exhibit continuity of low velocities across such an extensive region, this suggests that these features are not

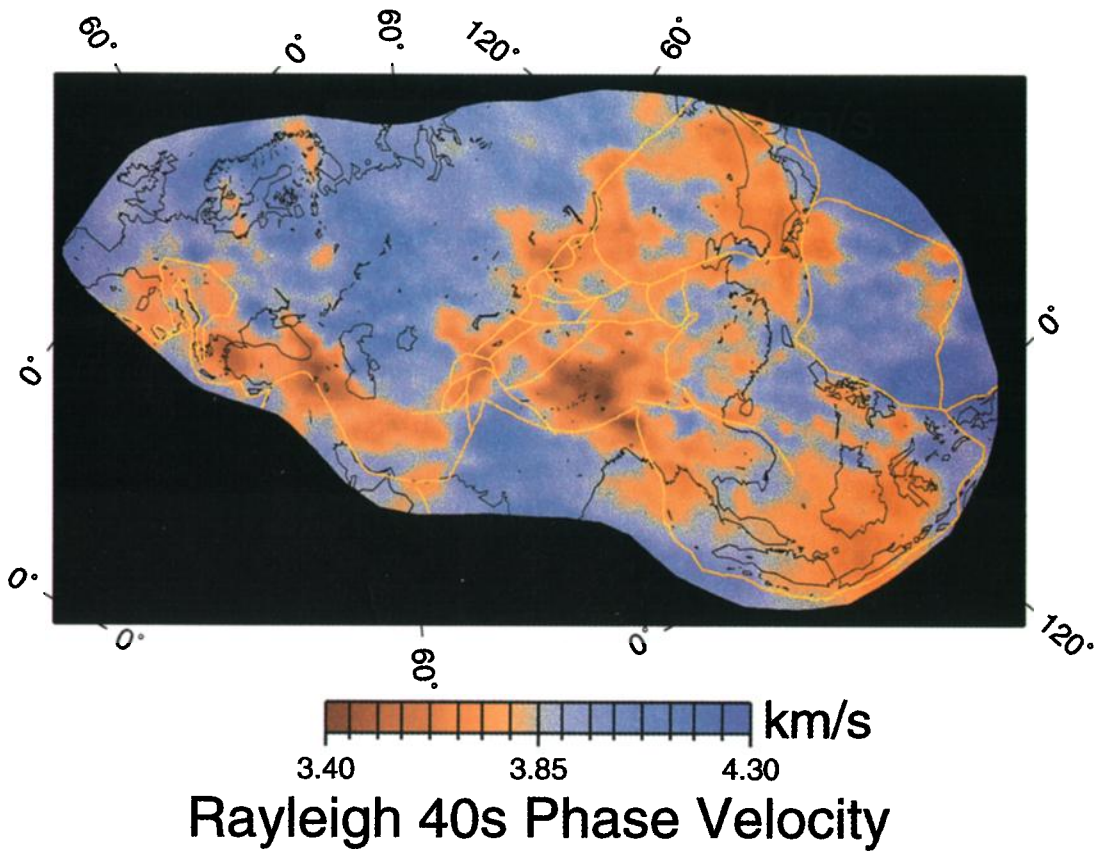
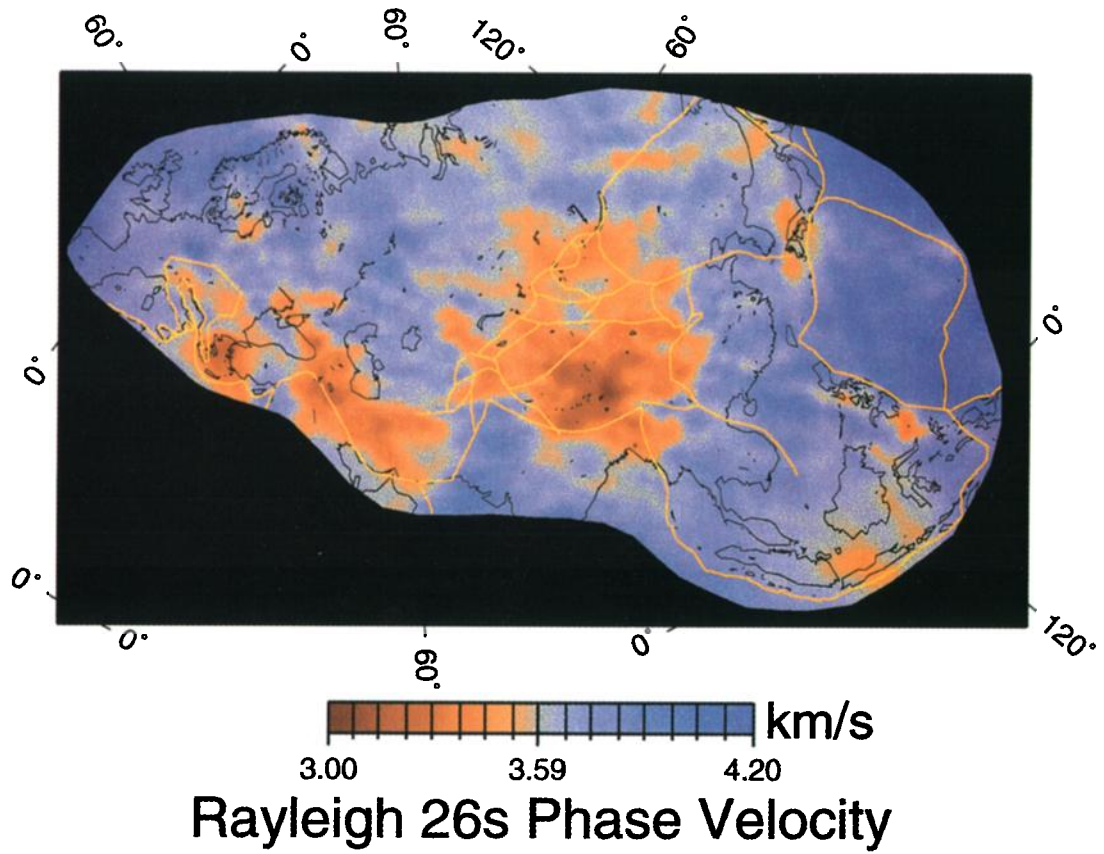
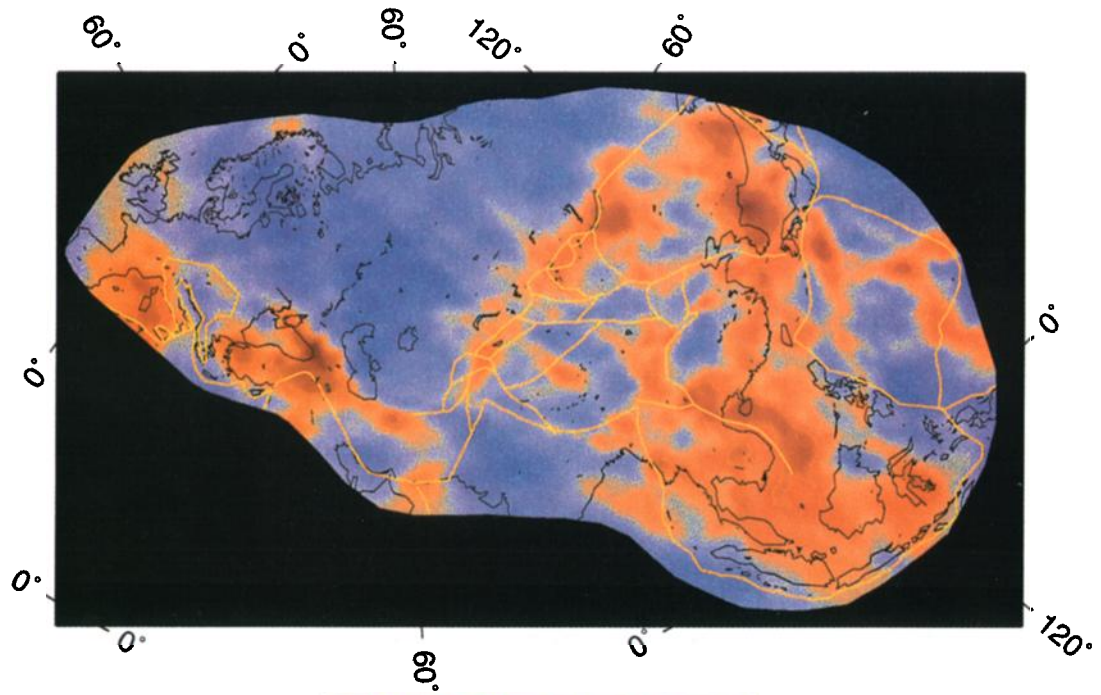
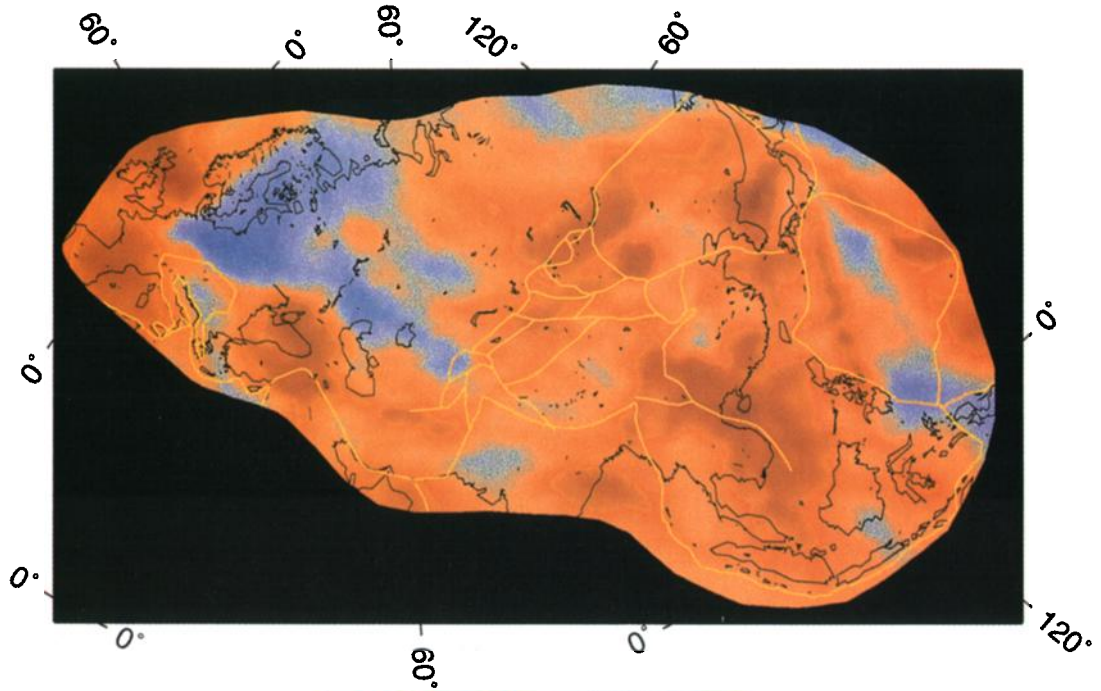


**Plate 5a.** Maps of Rayleigh wave phase velocity at periods 26 and 40 s. Tectonic boundaries shown are as in Plate 2.



3.70 4.00 4.30 km/s  
**Rayleigh 80s Phase Velocity**



4.00 4.40 4.80 km/s  
**Rayleigh 150s Phase Velocity**

**Plate 5b.** Same as Plate 5a, except for periods of 80 and 150 s.

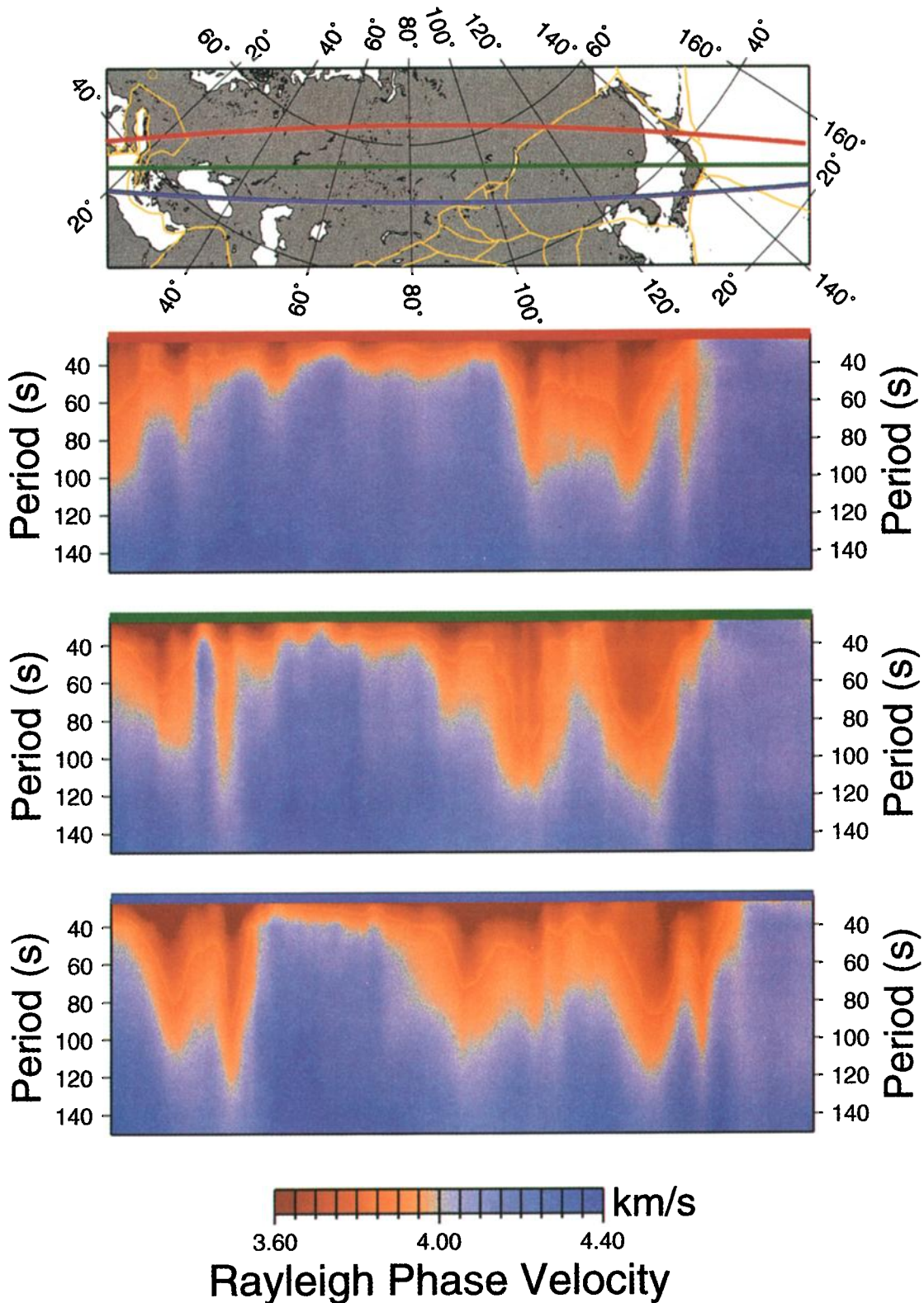


**Plate 6.** Fundamental mode Rayleigh wave phase velocity cross sections through Eurasia. Great circle paths are shown in the top plot, color coded with each phase velocity section shown below. In each column, the phase velocity sections contour the complete phase velocity curve between 26 and 150 s period below each point on the corresponding cross section. Since the sensitivity kernels for increasing periods of Rayleigh waves are dominantly sensitive to increasingly greater depths (Figure 6), these sections can be interpreted approximately as shear velocity slices with depth, with period-dependent vertical smoothing. The depth scale must be inferred from the sensitivity kernels. Tectonic boundaries shown are as in Plate 2. Notice that this interpretation scheme requires no inversion for shear velocity structure with depth and lies completely in the data space.

caused by thickening of the crust alone; instead, relatively low *SH* velocity mantle material must underlie all of these regions at least at the horizontal wavelengths imaged in this study.

As period increases from 80 s, phase velocities across areas outside of the mountainous regions gradually increase until at 150 s period the Love wave defines the East European platform and Baltic shield in western Eurasia and the western Siberian craton in eastern Eurasia by velocities which are around 10% higher than PEMc. These features are also seen on global maps of phase velocity [Trampert and Woodhouse, 1995, 1996; Ekström et al., 1997], but note that the increased resolution in this study shows that the high-velocity material of the East European platform extends northward across the Baltic shield to Finland but does not extend far into the Baltic Sea or into Norway or Sweden. A similar pattern can be observed between 80 and 200 km in the shear velocity models of Marquering and Snieder [1996] derived using full waveform inversion (although they map high velocities beneath the southernmost tip of Sweden). The high velocities observed in this study might be expected if the older cratonic and shield areas have cold, fast roots [e.g., Muzyert and Snieder, 1998], but what might not be expected is that the high velocities also seem to extend west of the northern Tornquist-Taisseyre zone, beneath the German-Polish depression (see also the 150 s Rayleigh wave velocities in Plate 5). Since the crust in this area is not anomalously thin [Mooney et al., 1998], this implies that relatively high velocities must exist in the lithosphere.

Turning our attention to the Rayleigh waves, the 26 s period velocities again show a strong correlation with regions of deformation but do not show the correlation with thick sedimentary cover which we observed in the 26 s Love map. This is explained by Figure 6, which shows that although the Rayleigh wave has a very shallow peak in its *SV* velocity sensitivity kernel, the main sensitivity is at a much deeper level which spans the lower crust and upper mantle even at the lowest periods we consider. Hence the low-period Rayleigh waves are sensitive to crustal thickness and hence indirectly to topography in the same manner as the 40 s Love wave. This is confirmed by the strong correlation between the 26 and 40 s Rayleigh wave phase velocities and the areas of highest topography shown in Plate 3 (upper plot).

This correlation continues through 60 s period, but by 80 s the Rayleigh wave is mainly sensitive to *SV* velocity structure around 120 km depth, well below the Moho transition. Notice that most of the low velocities beneath Tibet have disappeared at this period but strong low velocities still exist beneath the Baikal rift zone, the Caucasus-Aegean area, the western Mediterranean, and the Japanese Sea and within Indonesia, and these features persist as period increases toward 150 s. Over the period range 80–150 s, the peak sensitivity shifts from a depth of  $\sim 110$  km to  $\sim 220$  km with a large decrease in the sharpness of the peak. Hence the

persistence of these features indicates that either they are due primarily to the secondary peak sensitivity near the surface which exists for all periods (unlikely since the depth range of this peak is small) or the velocity anomalies are consistent over a large depth range ( $\sim 80$ –250 km).

Whereas we detected low Love 26 and 40 s phase velocities in the Zagros of southern Iran, with Rayleigh waves of period  $\geq 40$  s, we detect low velocities along the northern deformation margins in northern Iran. Also, whereas we observe two regions of low 26–80 s Love phase velocity in the NW Zagros/Caucasus and the SE Zagros, respectively, we detect almost continuous low 26 s Rayleigh wave velocities along the mountain chain. Hence, in the Zagros it appears that significant along-strike variations exist either in the *SH:SV* velocity ratio or in the depth extent of shear velocity anomalies.

Within the South China Sea, a low-velocity feature traces out the southeast side of the Red River and East Vietnam Boundary faults. Its peak is sharply defined for the 80 s Rayleigh data and becomes more diffuse at longer periods. This area is almost unsampled in most body wave studies since it is shallow and has accommodated few local earthquakes, and to our knowledge this feature has not been defined well enough to correlate with the faults in any previous studies. For this reason we analyze the origin of the low velocities in section 5.

Finally, notice the low-velocity anomalies located in north central Tibet in the 80 s Rayleigh velocity. This anomaly lies within the Chang Thang region of Tibet, an area of subrecent basaltic volcanism [Burke et al., 1974; Kidd, 1975; Pearce and Deng, 1988], poor upper mantle shear wave transmission [Barazangi and Ni, 1982; McNamara et al., 1994, 1997], and a pronounced upper mantle shear velocity lid structure [Brandon and Romanowicz, 1986; Curtis and Woodhouse, 1997]. This has led to the interpretation that the Chang Thang is an area of upwelling hot asthenospheric material causing partial melting in the uppermost mantle. The peak sensitivity of the 80 s Rayleigh phase velocity lies at around 110 km, and hence the observed low-velocity anomaly is consistent with the base of the high-velocity upper mantle lid having depth  $\leq \sim 100$  km (see section 5).

## 5. Discussion

In summary, we have applied fully automated signal processing techniques from global seismology to more than 30,000 horizontal and vertical component seismograms from earthquake-station pairs which lie within or on the plate boundaries enclosing Eurasia. In so doing, we avoid oceanic regions which are generally traversed by very long event-station paths and which deplete the resolution of global models appreciably. This allows us to attain increased resolution across Eurasia compared to that in global studies (compare Plates 2 and 3). Checkerboard style tests of resolution (Figure 5) and geographical correlations between our results and

known topographic features (Plates 1 and 3) suggest that we have produced phase velocity maps of Love and Rayleigh waves in the period range 26–100 s which resolve features of dimension  $>600$  km except in parts of central and far northern Eurasia and maps between 115 and 150 s with slightly lower resolution (features of dimension  $>750$  km should be resolved in the same areas as for the low-period maps). Maps of phase velocity are shown in Plates 3, 4 and 5.

In addition to the phase velocity maps, we produced a new one-dimensional model for the continent of Eurasia up to its surrounding plate boundaries, Eurasia1D, shown in Figure 4a. This shows that both Love and Rayleigh phase velocities at periods 26–150 s are lower on average across Eurasia than in the continental reference Earth model PEMc. By converting Eurasia1D phase velocities to group velocity we showed that it lies within 0.1 km/s of the one-dimensional model of average group velocity across approximately the same area obtained by *Ritzwoller and Levshin* [1998] using an entirely different approach, which included manual assessment of each measurement. This consistency suggests that neither our automated data selection criteria nor their operators who graded the group velocity measurements impose an absolute bias of more than 0.1 km/s on either study.

We have made various assumptions in carrying out this study, and each carries a risk of error, with additional sources of uncertainty caused by our reliance on other work and data. Our most limiting assumptions are as follows: while measuring and inverting phase velocities, we assume great circle propagation paths; hence there are no path bending and no simultaneous multipathed arrivals. Ray bending certainly does occur given the amplitude of velocity anomalies that we find and will cause possible mislocation of these anomalies and distort the amplitudes to some extent. Simultaneous multipathed arrivals would have an unknown, amplitude-dependent effect on the recorded phase, and hence we suspect that these might cause the largest errors in our measurements. Since these errors are likely to be geographically systematic, they may not average out when we perform our inversion, and since they are likely to be most prevalent at low periods, we recommend that the maps of 26 s period phase velocity are treated with more scepticism than the other maps.

We also assume that anisotropy does not affect the isotropic component of phase velocity. We have justified this to some extent by carrying out initial test inversions including azimuthal anisotropy in which we found that although improved data fit could be achieved by including anisotropic parameters, very little structural change occurred in the isotropic component [*Voskamp*, 1997]. Finally, we rely on centroid moment tensor (CMT) earthquake source descriptions and seismogram data from stations worldwide.

Our data set differs from the phase velocity data used by *Ekström et al.* [1997] or *van Heijst and Woodhouse*,

[1998] and the group velocity data used by *Ritzwoller and Levshin* [1998] in that we accept only results from seismograms which give robust measurements at all periods between 26 and 150 s. This is by far the most stringent condition in our data selection: at present, our database consists of 4020 Rayleigh and 4389 Love wave phase velocity dispersion curves, but tests show that if we apply our data selection criterion at each period independently (so that we accept results from the each seismogram in any period range in which the measurements seem robust), then we almost double the amount of data available for some periods. We prefer to accept less data for two reasons: First, if a seismogram provides poor estimates of phase velocity in some period range, this may be because of interfering multipathed arrivals which is a truly period-dependent effect, or it may be due to a station timing or response function error, to correlated data noise not detected by our definition of the signal to noise ratio, or to source mislocation. Any of the latter four possibilities will usually effect all periods of the seismogram whereas only a small period range may be “obviously” in error. Second, by creating a homogeneous data set across all periods it is possible for us to create approximately homogeneously resolved maps of phase velocity at all periods (ignoring, for the moment non-linear effects on the phase, like multipathing). In fact, we do not quite achieve this since we downweight a period-dependent number of outlying data by a factor of 2 in our final inversions, but we approximately preserve resolution at least across periods 26 to 100 s. This makes subsequent inversion of the set of phase velocity maps for shear velocity structure beneath each geographic location more meaningful (*Develee et al.*, submitted manuscript, 1998).

Mutual consistency between maps of different periods may also be illustrated by viewing the data set in a different way. Plates 6–9 each show three cross-sections through the Eurasian Rayleigh wave phase velocity space. Beneath each cross-section (red, green, and blue great circles) we plot the phase velocity at all periods modeled (26–150 s). In Plate 6 we plot absolute velocities whereas for Plates 7–9 we plot deviations from Eurasia1D. Thus, in the column beneath each geographical location, the complete Rayleigh phase velocity curve is contoured. Each period was inverted from the phase velocity data completely independently of the other periods; hence the lateral consistency in each section is due to the horizontal smoothing applied in the inversion (equation (9)), the vertical consistency is due to (1) the (weak) smoothing applied during the phase velocity measurement procedure (equations (13)–(15)), and (2) the fact that the data sets at each period were approximately consistent allowing us to use equal horizontal smoothing for each period.

Apart from the obvious improvements in ease of visualization, slices through phase velocity space like Plates 6–9 offer a further benefit: the sensitivity kernels in Figure 6 show that although they have some sensitiv-

ity to near-surface structure, the Rayleigh phase velocities are predominantly sensitive to shear velocity within a deeper, bounded depth range and the depth of the peak sensitivity increases with period. Hence Rayleigh phase velocity perturbations at short periods (e.g., 40 s) are caused mainly by shallow shear velocity heterogeneity (15–110 km), whereas those at long periods (150 s) are caused mainly by deeper structure (100–400 km). Thus the sections in Plates 6–9 at increasing period are roughly indicative of shear velocity variations at increasing depth but with period-dependent smoothing.

Many of the features on the sections may now be explained more easily. Moving from east to west along the profiles in Plate 6, initially all three sections show an oceanic signature of high phase velocities at low periods (compare PREM and PEMc in Figure 4a). Behind the subduction zone beneath Japan, the sections all show a very low velocity zone extending through all periods. In addition, this low-velocity zone is asymmetric; the Pacific side of the feature has a shallower dip than the continental side. This is due to the shallow ( $\sim 27^\circ$ ) westward dipping subducted oceanic slab beneath Japan which *van der Hilst et al.* [1991] locate at depths of 250–500 km beneath the Japanese Sea using  $P$  and  $pP$  wave travel times.

All three paths pass through tectonic boundaries in the continental interior. Notice that at each point where a boundary is crossed on each path, the section shows a low-velocity feature which extends to long periods. This is especially true of the localized feature beneath lake Baikal which presumably is detecting upwelling, hot asthenospheric material beneath the continental rift system. It is interesting to note, however, that the zone of most intense upwelling actually lies to the southeast of lake Baikal itself. Farther south the low velocity zone is wider, reflecting the increased width of the zone of deformation, with minimum velocities observed beneath the Altai mountains and Dzungaria. As each section traverses westward out of the zone of active deformation, the phase velocity structure becomes extremely stable with only minor fluctuations which might be attributed to crustal or sedimentary thickness variations. Such smooth, high-velocity structures might be expected in the stable continental interior.

As soon as each section crosses into the Carpathian–Alpine, Black Sea, or Caucasus regions, we again detect low-velocity features extending to long periods. The central section detects a localized velocity high beneath the Black Sea, possibly related to the oceanic nature of the region. Notice that the southern two sections traverse the Aegean region dissecting the subducting Mediterranean oceanic floor. In both cases we see a clear high velocity slab dipping northeastward beneath the low velocities at lower periods, in symmetry to the Japanese subduction zone.

Apart from the Baikal–Mongolian area, some of the lowest-velocity features lie directly beneath the Sea of

Japan and the Aegean. Both are areas of back arc extension. In the case of the Sea of Japan, the velocities are so low that they obscure the high velocity dipping slab due to smearing from intermediate to high periods. Inversions for shear velocity with depth will compensate for this effect, but for now the asymmetry of the low velocities is our main evidence for the existence of the dipping slab. Many velocity models constructed from body wave travel time anomalies show high-velocity dipping slabs beneath subduction zones, but these are always overlain (and often underlain) by a layer of low velocities. It is usually not clear whether the low-velocity layers are compensating for an average background velocity model which is too high (since most rays travel down slabs and hence travel faster than the average Earth) or whether they are real features [*Spakman et al.*, 1993]. In our study these velocities are certainly real since our background model does not suffer from the source of bias just mentioned, and in any case Plate 6 shows absolute velocities. Hence this study confirms the existence of low-velocity back arc areas, although the raw phase velocity measurements in their current form give little constraint on its depth extent.

In Plate 7 we show three more cross sections, this time as phase velocity anomalies to Eurasia1D, through the Tibetan plateau and surrounding regions and oriented due north, approximately the current direction of convergence of India with Eurasia. India subducts northward beneath the southern margin of Tibet and the Pamir, and Eurasia subducts southward beneath the northern margin of the Tien Shan. The lateral extent to which either plate subducts is unknown. Beneath the Pamir, subduction of both plates is steep and extends to several hundred kilometers depth as inferred from the seismicity patterns [*Burtman and Molnar*, 1993]. However, both subduction zones lie within a region  $\sim 300$  km across, and hence we can not resolve the dipping slabs. Instead, we observe very low velocities at short periods reflecting the Moho depth of around 70–80 km [*Holt and Wallace*, 1990; *Burtman and Molnar* 1993; *Curtis and Woodhouse* 1997]. In the central cross section we see that high velocities associated with the Indian shield appear to subduct beneath the Karakoram and Tibet at least up to the Altyn Tagh fault. The Tarim basin is underlain by high velocities [*Curtis and Woodhouse*, 1997] and the Tien Shan is an area of low velocities which extend further north at depth [see also *Roecker et al.*, 1993]. In the southern cross section we see very low phase velocities at low periods beneath the Tibetan plateau due to the 70–80 km crustal thickness, and these deepen appreciably beneath the Chang Thang area of north central Tibet [*Romanowicz*, 1982; *Brandon and Romanowicz*], 1986; *Curtis and Woodhouse*, 1997]. Note that although they are interrupted by a low-velocity feature at around  $23^\circ\text{N}$ , the higher velocities of the Indian shield seem to penetrate beneath the plateau up to the Chang Thang anomaly. The low-

velocity anomaly beneath the northern Indian shield in the lower section may be an artifact caused by our decrease in resolution south of the plateau, but it is in fact consistent with preliminary shear velocity models from a new global study which shows a decrease in the long-wavelength shear velocity between 100 and 200 km beneath this area [H. van Heijst and J. H. Woodhouse, manuscript in preparation, 1998]. Again, high phase velocities are observed beneath the Tarim basin, and low velocities are observed beneath the eastern Tien Shan. Note that the extent of subduction which we tentatively interpret from these sections is greater than that which may be inferred from the seismicity which only extends around 250 km north of the Himalayan thrust front.

The correlation of phase velocity anomalies with tectonic boundaries and terrains is investigated further in the next three sections through China, Indonesia, and the western Pacific and Philippine Sea (Plate 8). The top section crosses three major tectonic boundaries. In the south it crosses the East Vietnam Boundary (EVB) fault, the seaward extension of the Red River fault, a (currently) dextral strike-slip fault allowing eastward extrusion of south China from the India-Eurasia collision zone at a faster rate than that of Indochina [Peltzer and Tapponnier, 1988; Lee and Lawver, 1995]. Beneath Indochina we observe low, active continental-style phase velocities which deepen just east of the EVB fault in a band of low phase velocities at long periods which follow the northern side of the fault, as observed in Plate 5b. Through eastern China we see similar structure to that observed beneath Indochina, with alternating areas of increased and decreased velocity as we approach and traverse the Yellow Sea. The section then passes over the second tectonic boundary and into the zone of intense low back arc velocities observed in the first cross sections through Japan (Plate 6).

The second section again exhibits the low-velocity feature east of the EVB fault. To the south the structure is similar to that beneath Indochina, whereas to the north, slightly higher velocities are observed beneath the South China Sea. Low velocities are observed beneath the Yellow Sea with a high-velocity boundary beneath the tectonic fault before we enter the extreme low velocities of the Sea of Japan back arc region.

The low-velocity feature east of the EVB fault is different from the anomalies associated with many other boundaries in our models because it does not lie on the fault but beside it. It is also a relatively narrow feature which (because of its shape) appears to be associated with the fault itself (Plate 5b), whereas many other faults marked on our maps act as high-velocity boundaries between different low-velocity structures.

These features may be related to the Eocene to present-day tectonic activity associated with the Red River/EVB fault system. Between 44 and 20 Ma, collision between Greater India and Eurasia resulted in southeastward extrusion of Indochina with respect to the south China block, causing around 500 km of left-lateral shear across

the Red River fault [Tapponnier *et al.*, 1990]. Between 30 and 20 Ma, Indochina rotated clockwise by 18°, bending the EVB fault out of line with the Red River fault [Lee and Lawver, 1995]. The rotation caused SE Indochina to move to the SW with respect to the South China Sea, creating the SE trending Yinghai extensional basin offshore and along strike of the Red River fault. The creation of this basin shows that the concurrent N-S extension (rotating to NW-SE extension) in the South China Sea could not accommodate the SW relative movement of Indochina, so the crust around the boundary between the two plates extended and thinned. It is reasonable to conclude that the lithosphere must also have thinned, allowing hotter asthenospheric mantle material to flow upward providing a source of heat and probably inducing lithospheric partial melting.

Between 23 and 20 Ma, left-lateral motion ceased on the Red River fault, and by middle Miocene (15 Ma), right-lateral motion had begun as the maximum rate of Tibetan extrusion moved into south China [Tapponnier *et al.*, 1982; Wu *et al.*, 1989; Wang *et al.*, 1989] (the latter two are in Chinese and were reported by Lee and Lawver [1995]). By this time, extension in the South China sea had ceased. Hence, as Indochina moved NW with respect to south China, again the lithosphere to the east of Indochina must have been thinned to fill the space which would otherwise have been created, allowing further asthenospheric upwelling and lithospheric heating.

The low-velocity feature which we observe may be a consequence of either or both of these phases of upwelling and possible associated partial melting. This explanation would account for the fact that the low-velocity zone is observed mainly to the east and south-east of Indochina since during both phases the asthenospheric material would have filled the space trailing the block as it moved relative to the South China Sea.

The third section in Plate 8 passes through completely different types of structures. From the north, the section passes through the Pacific Ocean with very high velocities throughout the period range considered. It passes through the Bonin trench where the oceanic plate subducts to the southwest beneath the Philippine Sea; at this point a high-velocity feature is observed dipping down beneath the Philippine Sea. This feature is possibly associated with the subducting oceanic slab, but resolution in the Philippine Sea is poor (Figure 5), and we can draw no conclusions on this. Just before halfway across the section the path traverses the Palau-Kyushu ridge and immediately passes into old and fast oceanic lithosphere (exactly central on the section). It then passes through a fossil oceanic spreading center before traversing the zone of oceanic subduction beneath Indonesia along the Philippine trench, and again a dipping high-velocity slab is observed, this time beneath a low-velocity back arc in an area of high resolution (Figure 5).

Finally, as the section traverses NE Borneo, another

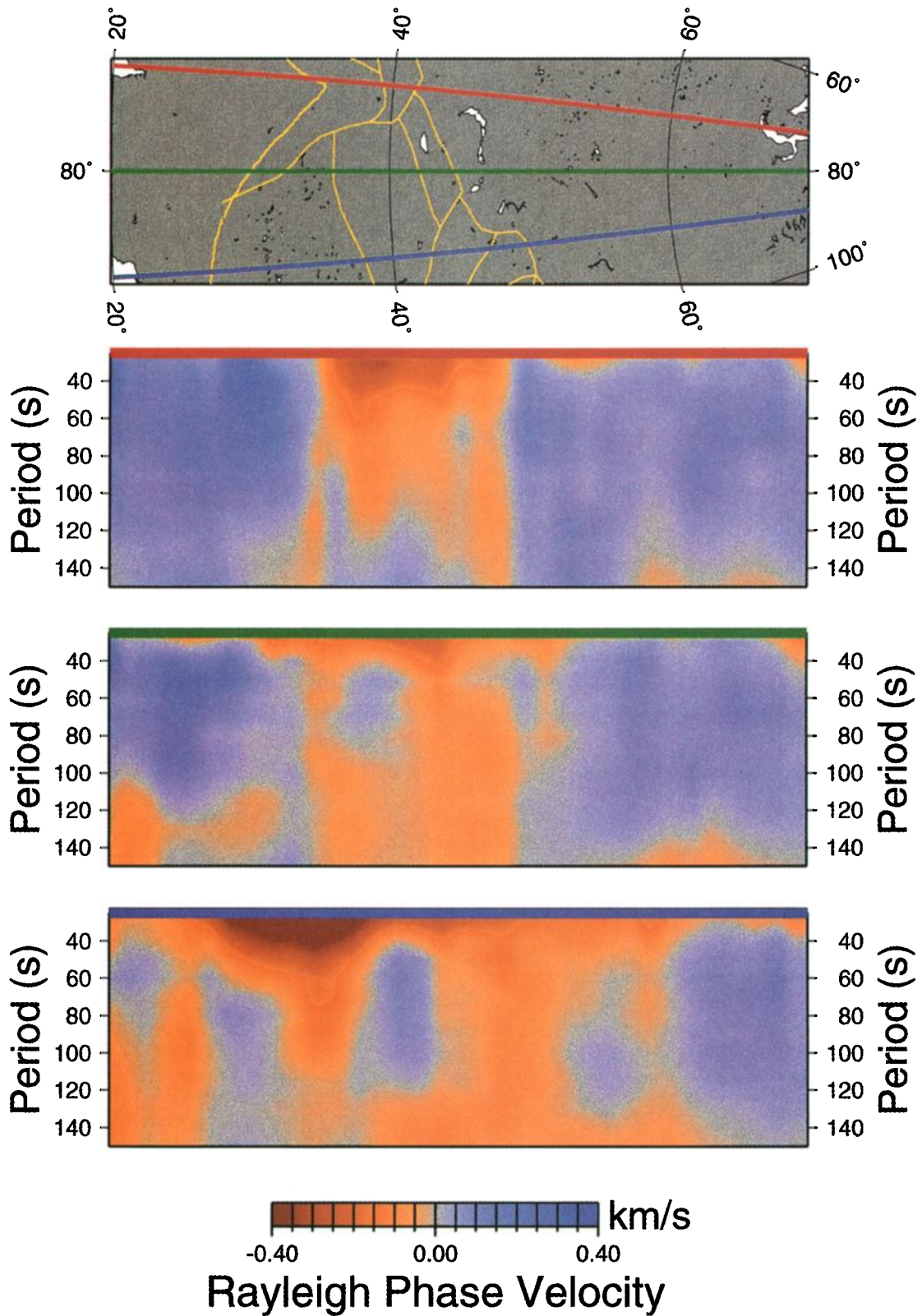


**Plate 7.** Similar plots to Plate 6, but Rayleigh wave phase velocity deviations from Eurasia1D (Figure 4a) are now shown through Tibet and the surrounding regions. Tectonic boundaries shown are as in Plate 2.

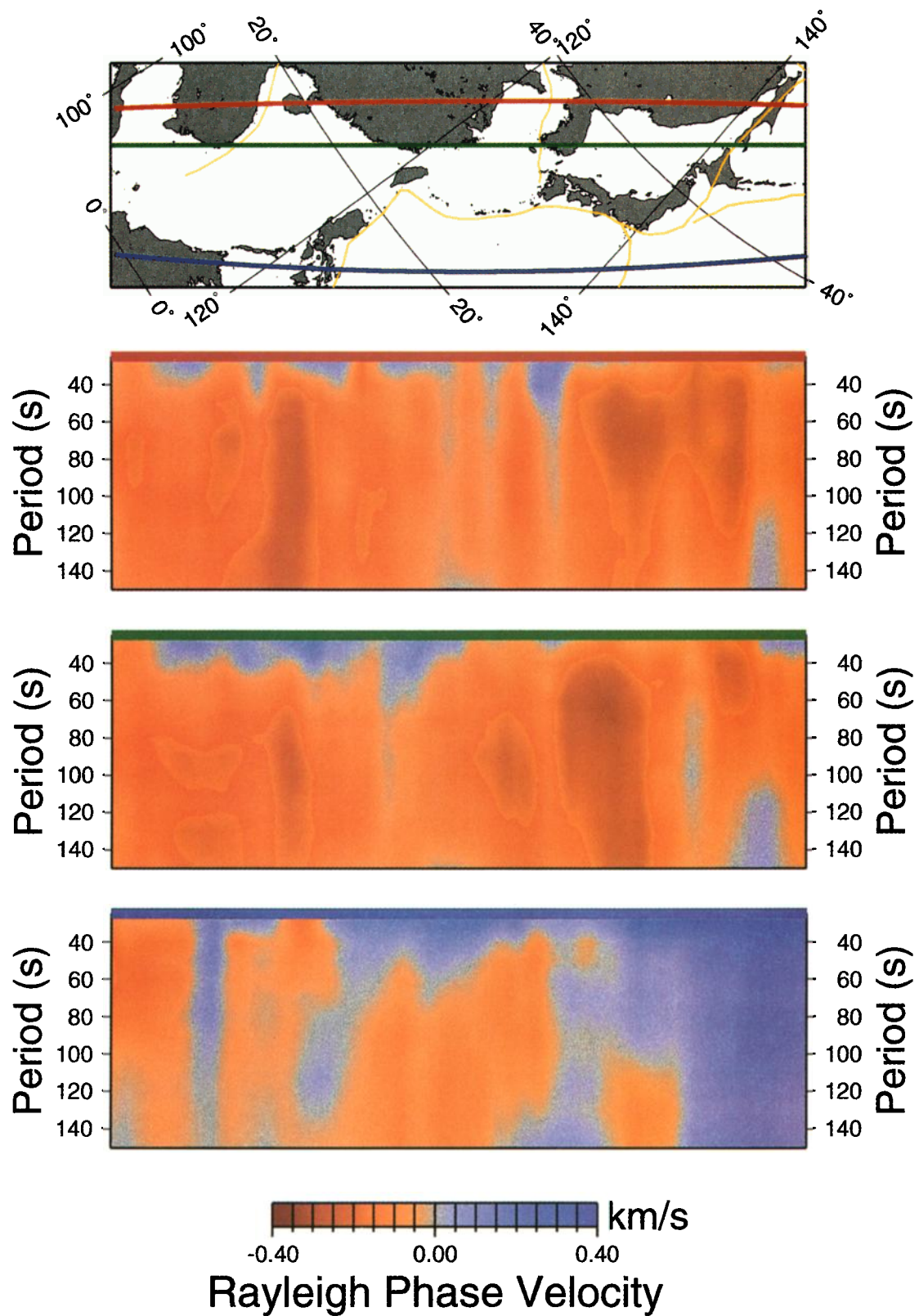


**Plate 8.** Similar plots to Plate 7, but Rayleigh wave phase velocity deviations are now shown through China, Indonesia, the Philippine Sea and the Pacific Ocean. Tectonic boundaries shown are as in Plate 2.

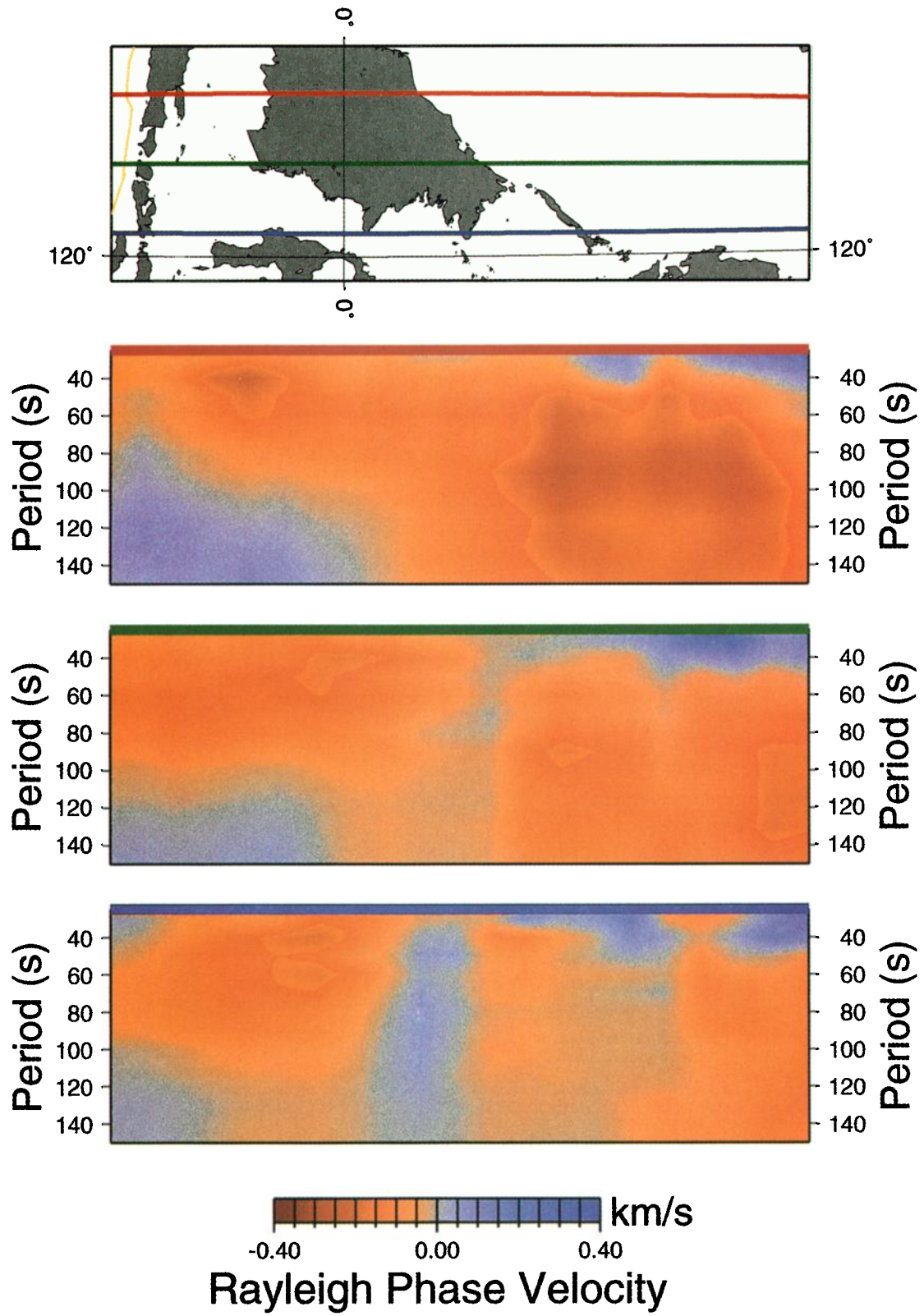


**Plate 9.** Similar plots to Plate 7, but Rayleigh wave phase velocity deviations are now shown through Borneo and the South China Sea. Tectonic boundaries shown are as in Plate 2.

very high velocity feature is observed before the low velocities beneath north Borneo. This feature is subvertical on this section, but Plate 9 shows three N-S sections through Borneo from which it appears that a slab has subducted southward beneath NE Borneo at a very steep angle, which is not visible beneath central Borneo. This subduction is not marked on any active tectonic maps, and there is very little seismicity beneath NE Borneo so subduction does not appear to be currently active. However, the existence of a high-velocity feature at the same location has been verified in the body wave tomography of H. Bijwaard and W. Spakman (submitted manuscript, 1998).

A fossil subducted slab in this area is most likely to be a relic of the early Eocene (50 Ma) to early Miocene (20 Ma) subduction of the proto-South China Sea. In fact, this subduction may have occurred along the whole of the north coast of Borneo between 50 and 30 Ma, but by 20 Ma only a small section of the proto-South China Sea remained, which was consumed beneath NE Borneo and the Sulu Sea by 15 Ma [Lee and Lawver, 1995].

As shown in all of the above examples, surface wave phase velocities can be used to image shallow Earth structure between zones of seismic activity (predominantly subduction zones), and in this way we image the volume which is unsampled in most body wave tomography. Hence observing dipping subduction zones using surface wave data is especially valuable because it allows the results of both types of study to be related more easily and included in joint interpretation. To our knowledge, this is the first time that dipping subduction zones have been observed in fundamental mode phase velocity maps. This again demonstrates the increased resolution available in the current study.

The detailed interpretations presented above are only possible because of the phase velocity slice visualization scheme. This in turn only makes sense because of the period-dependent consistency of our data set and due to the special nature of the fundamental mode Rayleigh phase velocity sensitivities. It is not as easy to use this scheme to interpret Love phase velocities or indeed group velocity maps since the latter are negatively sensitive to shear velocity in some depth ranges and positively sensitive in others (although the negative sensitivity may be sufficiently small that it can be ignored). The method is appealing since we are able to interpret the phase velocities, rather than some inversion of these for shear velocity structure with depth; such inversions always contain considerable nonuniqueness which is difficult to convey and display in a scientific paper, even in a linearized, Gaussian manner (see Devilee et al., submitted manuscript, 1998). However, to obtain quantitative bounds on the depth range of velocity anomalies, the subsequent inversion for shear velocity is necessary and will be the subject of a future study.

**Acknowledgments.** Thanks are extended to Anthony Lomax, Hendrik-Jan van Heijst, and Rob Devilee for many helpful discussions. We gratefully acknowledge the support

of John Woodhouse for the continued use of his jukebox data retrieval system and of the ORFEUS Data Center in Utrecht which supplied SPYDER data. The plots in this paper were created using GMT [Wessel and Smith, 1995]. This research was supported by the Netherlands Organization for Scientific Research (NWO) through Pionier project PGS 76-144.

## References

- Barazangi, M., and J. Ni, Velocities and propagation characteristics of  $P_n$  and  $S_n$  beneath the Himalayan arc and Tibetan plateau: Possible evidence for underthrusting of Indian continental lithosphere beneath Tibet, *Geology*, *10*, 179-185, 1982.
- Bourjot, L., and B. Romanowicz, Crust and upper mantle tomography in Tibet using surface waves, *Geophys. Res. Lett.*, *19*(9), 881-884, 1992.
- Brandon, C., and B. Romanowicz, A "no-lid" zone in the central Chang-Thang platform of Tibet: Evidence from pure path phase velocity measurements of long-period rayleigh waves, *J. Geophys. Res.*, *91*(B6), 6547-6564, 1986.
- Burke, K., J. F. Dewey, and W. S. F. Kidd, The Tibetan plateau: Its significance for tectonics and petrology, *Geol. Soc. Am. Abstr. Programs*, *6*, 1027-1028, 1974.
- Burtman, V. S., and P. Molnar, Geological and geophysical evidence for deep subduction of continental crust beneath the Pamir, *Spec. Pap. Geol. Soc. Am.*, *281*, 1-76, 1993.
- Cara, M., Filtering of dispersed wavetrains, *Geophys. J. R. Astron. Soc.*, *33*, 65-80, 1973.
- Curtis, A., and J. H. Woodhouse, Crust and upper mantle shear velocity structure beneath the Tibetan plateau and surrounding regions from interevent surface wave phase velocity inversion, *J. Geophys. Res.*, *102*(B8), 11789-11813, 1997.
- Curtis, A., R. Devilee, K. Roy-Chowdhury, and R. Snieder, Shear wave velocity structure and crustal thickness beneath Eurasia inverted from surface wave dispersion using neural networks, *Eos Trans. AGU*, *78*(17), Spring Meet. Suppl., S212, 1997.
- Dziewonski, A. M., and D. L. Anderson, Preliminary reference Earth model, *Phys. Earth Planet. Inter.*, *125*, 297-356, 1981.
- Dziewonski, A. M., S. Bloch, and M. Landisman, A technique for the analysis of transient seismic signals, *Bull. Seismol. Soc. Am.*, *59*(1), 427-444, 1969.
- Dziewonski, A. M., A. L. Hales, and E. R. Lapwood, Parametrically simple Earth models consistent with geophysical data, *Phys. Earth Planet. Inter.*, *10*, 12-48, 1975.
- Ekström, G., J. Tromp, and E. W. F. Larson, Measurements and global models of surface wave propagation, *J. Geophys. Res.*, *102*(B4), 8137-8157, 1997.
- Grand, S. P., and D. V. Helmberger, Upper-mantle shear structure beneath Asia from multi-bounce  $S$ -waves, *Phys. Earth Planet. Inter.*, *41*, 154-169, 1985.
- Holt, W. E., and T. C. Wallace, Crustal thickness and upper mantle velocities in the Tibetan plateau region from the inversion of regional  $P_n$  waveforms: Evidence for a thick upper mantle lid beneath southern Tibet, *J. Geophys. Res.*, *95*(B8), 12,499-12,525, 1990.
- Jackson, J., and D. McKenzie, Active tectonics of the Alpine-Himalayan belt between western Turkey and Pakistan, *Geophys. J. R. Astron. Soc.*, *77*, 185-264, 1984.
- Kidd, W. S. F., Widespread late Neogene and Quaternary calc-alkaline volcanism on the Tibetan plateau, *Eos Trans. AGU*, *56*(6), 453, 1975.
- Lancaster, P., and K. Salkauskas, *Curve and Space Fitting: An Introduction*, Academic San Diego, Calif., 1986.
- Landisman, M., A. Dziewonski, and Y. Satō, Recent im-

- provements in the analysis of surface wave observations, *Geophys. J. R. Astron. Soc.*, *17*, 369–403, 1969.
- Lee, T.-Y., and L. A. Lawver, Cenozoic plate reconstruction of Southeast Asia, *Tectonophysics*, *251*, 85–138, 1995.
- Lyon-Caen, H., Comparison of the upper mantle shear wave velocity structure of the Indian shield and the Tibetan plateau and tectonic implications, *Geophys. J. R. Astron. Soc.*, *86*, 727–749, 1986.
- Marquering, H., and R. Snieder, Surface-wave velocity structure beneath Europe, the northeastern Atlantic and western Asia from waveform inversion including surface-wave mode coupling, *Geophys. J. Int.*, *127*, 283–304, 1996.
- McNamara, D. E., T. J. Owens, P. G. Silver, and F. T. Wu, Shear wave anisotropy beneath the Tibetan plateau, *J. Geophys. Res.*, *99*(B7), 13,655–13,665, 1994.
- McNamara, D. E., W. R. Walters, T. J. Owens, and C. J. Ammon, Upper mantle velocity structure beneath the Tibetan plateau from  $P_n$  travel time tomography, *J. Geophys. Res.*, *102*(B1), 493–505, 1997.
- Mooney, W. D., G. Laske, and T. G. Masters, CRUST 5.1: A global crustal model at  $5^\circ \times 5^\circ$ , *J. Geophys. Res.*, *103*(B1), 727–747, 1998.
- Morelli A. (ed.), A., 1994 status report of the Federation of Digital Seismographic Networks, *Ann. Geofis.*, *37*(5), 1037–1112, 1994.
- Muyzert, E., and R. Snieder, A seismic cross section through the east European continent, *Geophys. J. Int.*, in press, 1998.
- Paige, C. C., and M. A. Saunders, LSQR: An algorithm for sparse linear equations and sparse least squares, *ACM Trans. Math. Soft.*, *8*, 43–71, 1982.
- Pearce, J. A., and W. Deng, The ophiolites of Tibet geotransverses Lhasa to Golmud (1985) and Lhasa to Kathmandu (1986), *Philos. Trans. R. Soc. London, Ser. A*, *327*, 215–238, 1988.
- Peltzer, G., and P. Tapponnier, Formation and evolution of strike-slip faults, rifts, and basins during the India-Asia collision: An experimental approach, *J. Geophys. Res.*, *93*, 15,085–15,117, 1988.
- Pines, I., T.-L. Teng, and R. Rosenthal, A surface wave dispersion study of the crustal and upper mantle structure of China, *J. Geophys. Res.*, *85*(B7), 3829–3844, 1980.
- Ritzwoller, M. H., and A. L. Levshin, Eurasian surface wave tomography: Group velocities, *J. Geophys. Res.*, *103*(B3), 4839–4878, 1998.
- Roecker, S. W., T. M. Sabitova, L. P. Vinnik, Y. A. Burmakov, M. I. Golvanov, R. Mamatkanova, and L. Munirova, Three-dimensional elastic wave velocity structure of the western and central Tien Shan, *J. Geophys. Res.*, *98*(B9), 15779–15795, 1993.
- Romanowicz, B., Constraints on the structure of the Tibetan plateau from pure path phase velocities of Love and Rayleigh waves, *J. Geophys. Res.*, *87*(B8), 6865–6883, 1982.
- Spakman, W., S. Van Der Lee, and R. van der Hilst, Travel-time tomography of the European–Mediterranean mantle down to 1400 km, *Phys. Earth Planet. Inter.*, *79*, 3–74, 1993.
- Tapponnier, P., G. Peltzer, A. Y. Le Dain, and R. Armijo, Propagating extrusion tectonics in Asia: New insights from simple experiments with plasticine, *Geology*, *10*, 611–616, 1982.
- Tapponnier, P., R. Lacassin, P. H. Leloup, U. Schärer, D. Zhou, H. Wu, X. Liu, S. Ji, L. Zhang, and J. Zhong, The Ailao Shan/Red River metamorphic belt: Tertiary left-lateral shear between Indochina and south China. *Nature*, *343*, 431–437, 1990.
- Tarantola, A., and B. Valette, Inverse problems = quest for information, *J. Geophys.*, *50*, 159–170, 1982.
- Trampert, J., and R. Snieder, Model estimations based on truncated expansions: Possible artifacts in seismic tomography, *Science*, *271*, 1257–1260, 1996.
- Trampert, J., and J. H. Woodhouse, Global phase velocity maps of Love and Rayleigh waves between 40 and 150 seconds, *Geophys. J. Int.*, *122*, 675–690, 1995.
- Trampert, J., and J. H. Woodhouse, High resolution global phase velocity distributions, *Geophys. Res. Lett.*, *23*(1), 21–24, 1996.
- van der Hilst, R. D., E. R. Engdahl, and W. Spakman, Tomographic inversion of  $P$  and  $PP$  data for aspherical mantle structure below the northwest Pacific Region, *Geophys. J. Int.*, *114*, 264–302, 1993.
- van Heijst, H., and J. H. Woodhouse, Measuring surface wave overtone phase velocities using a mode branch stripping technique, *Geophys. J. Int.*, in press, 1998.
- Voskamp, J. A., Azimuthal dependence of surface wave phase velocities across the Eurasian continent, *Graduate thesis, Utrecht University, Netherlands*, 1997.
- Wang, X., J. Yan, and J. Lin, The inverted structure and its significance in petroleum geology (in Chinese with English abstract), *Earth Sci. J. China Univ. Geosci.*, *101–108*, 1989.
- Wessel, P., and W. H. F. Smith, New version of the generic mapping tools released, *Eos Trans. AGU*, *72*, 329, 1995.
- Woodhouse, J. H., and A. M. Dziewonski, Mapping the upper mantle: Three-dimensional modeling of Earth structure by inversion of seismic waveforms, *J. Geophys. Res.*, *89*, 5953–5986, 1984.
- Wu, H., Zhang, L. and Ji, S., The red river–ailaoshan fault zone — himalayan large sinistral strike-slip intracontinental shear zone, *Sci. Geol. Sin.*, *1–8* (in Chinese with English abstract), 1989.
- Zang, Y. S., and T. Tanimoto, High resolution global upper mantle structure and plate tectonics, *J. Geophys. Res.*, *98*, 9793–9823, 1993.
- Zhao, L.-S., A. Hasegawa, and S. Hirouchi, Tomographic imaging of  $P$  and  $S$  wave velocity structure beneath northeastern Japan, *J. Geophys. Res.*, *97*, 19,909–19,928, 1992.
- Zhao, L.-S., D. V. Helmberger, and D. G. Harkrider, Shear-velocity structure of the crust and upper mantle beneath the Tibetan plateau and southeastern China, *Geophys. J. Int.*, *105*, 713–730, 1991.
- Zielhuis, A., and G. Nolet, Shear-wave velocity variations in the upper mantle beneath central Europe, *Geophys. J. Int.*, *117*, 695–715, 1994.
- Zonenshain, L. P., and L. A. Savostin, Geodynamics of the Baikal rift zone and plate tectonics of Asia, *Tectonophysics*, *76*, 133–171, 1981.
- Zonenshain, L. P., M. I. Kuzmin, and B. M. Page, *Geology of the USSR: A Plate-Tectonic synthesis*, *Geodyn. Ser.*, vol. 21, AGU, Washington, D. C., 1990.

A. Curtis, Schlumberger Cambridge Research, High Cross, Madingley Road, Cambridge CB3 0EL, England. (email: curtis@cambridge.scr.slb.com)

B. Dost, ORFEUS Data Center, P.O. Box 201, 3730 AE De Bilt, Netherlands.

R. Snieder, J. Trampert, Department of Theoretical Geophysics, Utrecht University, Budapestlaan 4, Postbus 80.021, 3508 TA Utrecht, Netherlands.

(Received September 19, 1997; revised February 25, 1998; accepted March 6, 1998.)